Simulated Mid-Holocene and Last Interglacial Climate Using Two Generations of AWI-ESM

XIAOXU SHI,[a] MARTIN WERNER,[a] QIANG WANG,[a] HU YANG,[a] AND GERRIT LOHMANN[a]

[a] *Alfred Wegener Institute, Helmholtz Center for Polar and Marine Research, Bremerhaven, Germany*

(Manuscript received 13 May 2022, in final form 26 July 2022)

ABSTRACT: Numerical simulations allow us to gain a comprehensive understanding of the underlying mechanisms of past, present, and future climate changes. The mid-Holocene (MH) and the last interglacial (LIG) were the two most recent warm episodes of Earth's climate history and are the focus of paleoclimate research. Here, we present results of MH and LIG simulations with two versions of the state-of-the-art Earth system model AWI-ESM. Most of the climate changes in MH and LIG compared to the preindustrial era are agreed upon by the two model versions, including 1) enhanced seasonality in surface temperature that is driven by the redistribution of seasonal insolation; 2) a northward shift of the intertropical convergence zone (ITCZ) and tropical rain belt; 3) a reduction in annual mean Arctic sea ice concentration; 4) weakening and northward displacement of the Northern Hemisphere Hadley circulation, which is related to the decrease and poleward shift of the temperature gradient from the subtropical to the equator in the Northern Hemisphere; 5) a westward shift of the Indo-Pacific Walker circulation due to anomalous warming over the Eurasia and North Africa during boreal summer; and 6) an expansion and intensification of Northern Hemisphere summer monsoon rainfall, with the latter being dominated by the dynamic component of moisture budget (i.e., the strengthening of wind circulation). However, the simulated responses of the Atlantic meridional overturning circulation (AMOC) in the two models yield different results for both the LIG and the MH. AMOC anomalies between the warm interglacial and preindustrial periods are associated with changes in North Atlantic westerly winds and stratification of the water column at the North Atlantic due to changes in ocean temperature, salinity, and density.

KEYWORDS: Paleoclimate; Climate models; Model comparison

1. Introduction

The mid-Holocene [MH; around 6000 years ago (6 ka)] and the last interglacial (LIG; around 127 ka) were the two most recent warm periods during the Quaternary. They are characterized by increased seasonality as compared to today due to the differences in Earth's astronomical configuration (i.e., eccentricity, obliquity, and precession). These parameters govern the motion of Earth, and shape the seasonal and latitudinal distribution of solar radiation received at the top of the atmosphere (Berger 1977). In comparison to the present day, the radiative forcing over the Northern Hemisphere was stronger in boreal summer and weaker in boreal winter during the MH and the LIG. In the LIG, this effect is substantially stronger due to a more elliptical Earth orbit than during the MH (Lunt et al. 2013; Pfeiffer and Lohmann 2016). The significant changes in seasonal cycle in both MH and LIG relative to the preindustrial (PI) period are superimposed by a minor cooling associated with lower atmospheric greenhouse gas concentrations (Köhler et al. 2017).

MH and LIG are of particular interest to paleoclimate researchers (Yin and Berger 2015). The climates of MH and LIG have been examined in a large number of studies with the use of reconstruction records. Due to the warmer climate over the Northern Hemisphere, there was less Arctic sea ice cover during the MH relative to the present, evidenced in sediment cores (Hanslik et al. 2010) and driftwood (Funder et al. 2011) as well as biomarkers (Müller et al. 2012). Indicated by pollen proxy and plant macrofossils, in the MH there was higher precipitation compared to the present day across Eurasia, North America, and China as well as in the Mediterranean region (Bartlein et al. 2011). Pronounced wetter conditions were also documented over northern Africa relative to today (Bartlein et al. 2011). The strengthened summer monsoon rainfall over the Northern Hemisphere monsoon domains in the MH is also indicated by high-resolution speleothem records (Y. Wang et al. 2008). The stable water isotopes as recorded in the Greenland ice cores imply a higher temperature (by 5 K) during the LIG than today (North Greenland Ice Core Project members 2004). In terms of LIG precipitation, there is relatively limited documentation based on terrestrial archives. Scussolini et al. (2019) gives a clear picture from the existing proxy database of a wetter LIG over most parts of the Northern Hemisphere continents as compared to today. Similarly, reconstruction records imply a pronounced enhancement of East Asian monsoon in the LIG with respect to the present (Y. Wang et al. 2008). During both MH and LIG, the Sahara featured multiple types of vegetation, as well as lakes and rivers that are not evident today (Drake et al. 2011; Skonieczny et al. 2015).

Although reconstruction records can document the signals of the past climate, due to their limited quantity and rather coarse temporal and spatial coverage it is still a challenge for us to have a global view of the past climate and to explore the

Denotes content that is immediately available upon publication as open access.

Corresponding author: Xiaoxu Shi, xshi@awi.de

DOI: 10.1175/JCLI-D-22-0354.1

© 2022 American Meteorological Society. For information regarding reuse of this content and general copyright information, consult the AMS Copyright Policy (www.ametsoc.org/PUBSReuseLicenses).

Unauthenticated | Downloaded 12/20/22 12:13 PM UTC

TABLE 1. PMIP4 boundary conditions for preindustrial, mid-Holocene, and last interglacial.

Experiment	CO_2 (ppm)	CH_4 (ppb)	N_2O (ppb)	Eccentricity	Obliquity	Perihelion − 180°
PI	284.3	808.2	273	0.016764	23.459°	100.33°
MH	264.4	597	262	0.018682	24.105°	0.87°
LIG	275	685	255	0.039378	24.040°	275.41°

underlying mechanisms of Earth's system only based on the existing proxy database. Numerical simulations, thus, provide us the opportunity to examine the past climate more comprehensively and also help us better predict the climate of the future. Particularly, the Paleoclimate Model Intercomparison Project (PMIP4) brings together different modeling groups, providing the possibility to synthesize results from different models (Otto-Bliesner et al. 2017; Kageyama et al. 2018, 2021b). As the focus of PMIP4, the climates of MH and LIG have been examined by a large number of studies (Brierley et al. 2020; Otto-Bliesner et al. 2021; Kageyama et al. 2021a). Due to Earth's orbital parameter anomalies with respect to the present, Earth in the periods of MH and LIG receives more insolation in summer and less in winter, leading to enhanced seasonal cycles in the two time periods (Kukla et al. 2002; Shi and Lohmann 2016; Shi et al. 2020; Zhang et al. 2021; Kageyama et al. 2021a). Arctic amplification and sea ice loss during the MH helps to strengthen the Northern Hemisphere warming (Park et al. 2019). Climate simulations also identified a northward displacement of the intertropical convergence zone (ITCZ) during the two warm periods, as well as a broadening in monsoon domain for the Northern Hemisphere (Jiang et al. 2015; Braconnot et al. 2007; Nikolova et al. 2012; Fischer and Jungclaus 2010). Simulations without dynamic vegetation indicate that the increased Northern Hemisphere seasonal cycle is the main driver of the "Green Sahara" during the MH and LIG (Kutzbach and Liu 1997). However, using models equipped with dynamic vegetation, Lu et al. (2018) and Hopcroft et al. (2017) reveal that the MH Sahara was significantly wetter than previously assumed, suggesting that vegetation coverage itself also plays an important role in humidification of the Sahara.

Model resolution is found to be an important factor influencing simulated results (Shi and Lohmann 2016; Shi et al. 2020). In simulations with either high or low spatial resolution, the change of the Atlantic meridional overturning circulation (AMOC) in the MH as compared to the present has opposite sign (Shi and Lohmann 2016). Specifically, in simulations using ECHAM6-FESOM and MPIESM, low-resolution runs lead to a weaker MH AMOC compared to PI, while stronger MH AMOC than PI is simulated in the high-resolution experiments. Such discrepancy is attributed to different changes in MH-PI Labrador Sea density in low- and high-resolution simulations. The same results can also be seen when comparing results of FGOALS-g2 and FGOALS-s2 (Shi and Lohmann 2016). Among the PMIP models, AWI-ESM-1-1-LR and AWI-ESM-2-1-LR have unstructured-grid ocean components and are both configured with high oceanic resolutions of up to 25 km at high latitudes and 35 km at coastal areas and the tropical belt. In the present study, we perform PI, MH, and LIG experiments using these two model versions. The boundary conditions are prescribed according to the PMIP4 protocol (Otto-Bliesner et al. 2017). The purpose of this paper is to document the Alfred Wegener Institute (AWI) contribution to PMIP4 using the two model versions. We will identify the major features of MH and LIG climate as simulated by both model versions, and the information can thus be further used for intermodel and model–data comparisons. Our results can also help PMIP4 users to understand the past climate changes from the perspective of high-resolution simulations.

The structure of the paper is as follows: In section 2, we describe the models employed in our study and provide detailed information on our experimental design. Section 3 presents the results on how the MH and LIG climates differ from today. We summarize and conclude in section 4.

2. Methodology

a. Model description

In the present study, simulations are performed with two state-of-the-art Earth system models developed at the Alfred Wegener Institute: AWI-ESM-1-1-LR (hereafter referred to as AWIESM1) and AWI-ESM-2-1-LR (hereafter referred to as AWIESM2). They share the same atmospheric module, ECHAM6, mainly established by the Max Planck Institute for Meteorology (MPI-M). The ocean–sea ice component of AWIESM1 is the first release of the Finite Element Sea Ice-Ocean Model (FESOM1.4), while AWIESM2 employs an upgraded version (FESOM2) that builds upon FESOM1.4 but with a dynamical core based on the finite-volume formulation. Both model versions have been validated (Sidorenko et al. 2015; Rackow et al. 2018; Sidorenko et al. 2019) and widely used in understanding the climate changes in the past (Yang et al. 2022b; Lohmann et al. 2020; Kageyama et al. 2021b; Brierley et al. 2020; Otto-Bliesner et al. 2021; Renoult et al. 2020), present, and future (Yang et al. 2020b, 2022a; Shi and Lohmann 2017). More details of the AWIESM1 and AWIESM2 components are described in the following subsections.

1) ECHAM6

ECHAM6 is the sixth generation of the atmospheric general circulation model ECHAM developed at the Max Planck Institute for Meteorology (Stevens et al. 2013). The model contains a complete representation of atmospheric physical processes from the surface to 0.01 hPa (about 80 km). The model utilizes a Gaussian grid for physical representation and computation of nonlinear equation terms. The subgrid orography approach presented in Lott (1999) is used to configure momentum transport derived from boundary effects.

Unauthenticated | Downloaded 12/20/22 12:13 PM UTC

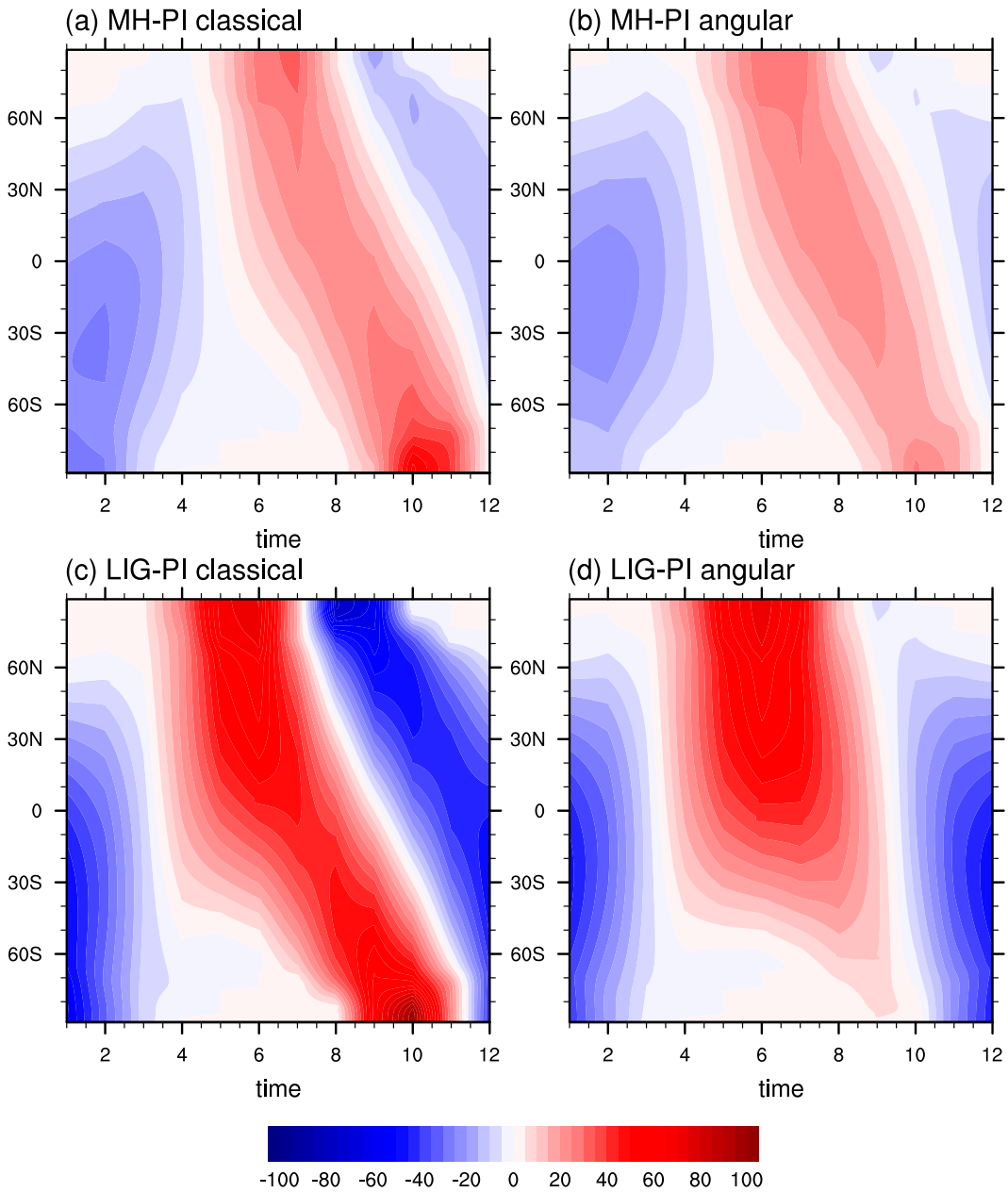

FIG. 1. Monthly mean insolation (W m^{-2}) at the top of the atmosphere as a function of latitude and time (month) for (a) MH minus PI based on the classical calendar, (b) MH minus PI based on the angular calendar, (c) LIG minus PI based on the classical calendar, and (d) LIG minus PI based on the angular calendar.

The model's dynamics are determined by hydrostatic primitive equations. A land surface component, JSBACH, is included in the model, which represents multiple plant functional types and two bare surface types (Loveland et al. 2000; Raddatz et al. 2007). The atmospheric water tracers in ECHAM6, which are in gaseous, liquid, and solid phases, are advected horizontally with the flux-form semi-Lagrangian scheme described in Lin and Rood (1996). An eddy diffusion method is employed for vertical diffusion of tracers (Garratt 1992), which can also be caused by moist convection. The moist convection is calculated using the Tiedtke–Nordeng scheme (Tiedtke 1989; Nordeng 1994) where a distinction is made for deep, midlevel, and shallow convections (Möbis and Stevens 2012).

2) FESOM1.4 AND FESOM2.0

FESOM1.4 is a hydrostatic ocean circulation model discretized on an unstructured grid with a continuous conforming representation of model variables (Danilov et al. 2004; Q. Wang et al. 2008; Timmermann et al. 2009; Wang et al. 2014; Sidorenko et al. 2015). A spatial-variable resolution is

Unauthenticated | Downloaded 12/20/22 12:13 PM UTC

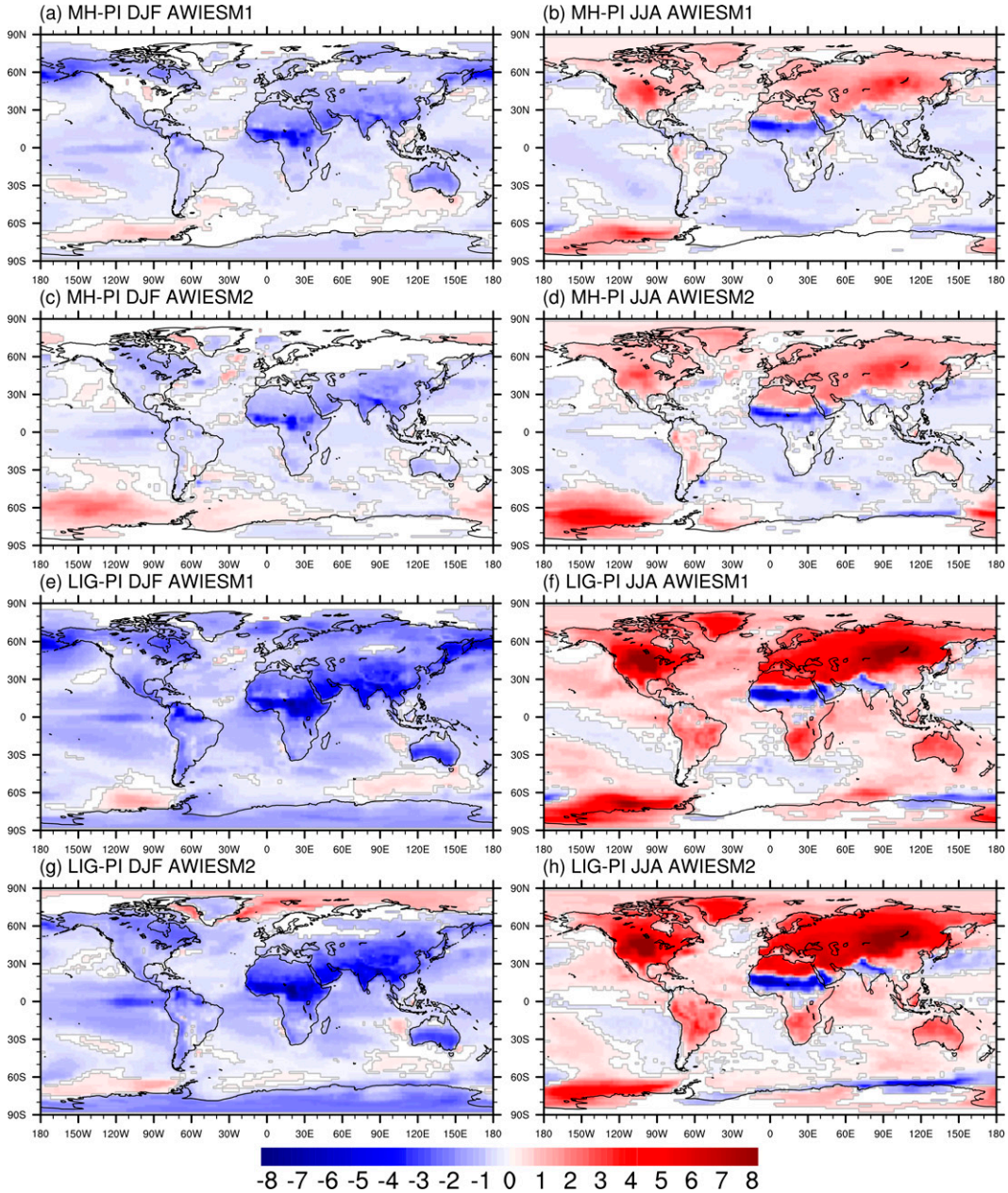

FIG. 2. Simulated anomalies of surface temperature (K) between MH and PI in (a),(c) DJF and (b),(d) JJA, based on AWIESM1 in (a) and (b) and AWIESM2 in (c) and (d). (e)–(h) As in (a)–(d), but for the surface temperature anomalies between LIG and PI. Only anomalies with significance levels larger than 95% based on Student's *t* test are shown.

applied with up to 25 km over the high latitudes and 35 km at coastal regions. The model also has a refined resolution over the equatorial belt (up to 35 km). A spherical coordinate system is adopted in the model with the poles locating at the Greenland and the Antarctic continent in order to avoid convergence of meridians in the computational domain. The sea ice component of FESOM1.4 is discretized on the same unstructured grid as the ocean model (Danilov et al. 2015) and uses the thermodynamics of Parkinson and Washington (1979). Subgrid-scale ocean parameterizations (Redi 1982; Gent and McWilliams 1990), the elastic-viscous-plastic (EVP) sea ice rheology (Hunke and Dukowicz 1997), and a prognostic snow layer (Owens and Lemke 1990), as well as zero-layer sea ice thermodynamics (Semtner 1976), have been implemented in the model. In terms of the vertical mixing, the *k*-profile parameterization (KPP) as described in Large et al. (1994) is implemented. The stand-alone FESOM1.4 has been validated with prescribed atmospheric forcing by Timmermann et al. (2009), Scholz et al. (2013), and Wang et al. (2014), and through the CORE-II project (e.g., Danabasoglu et al. 2014).

Unauthenticated | Downloaded 12/20/22 12:13 PM UTC

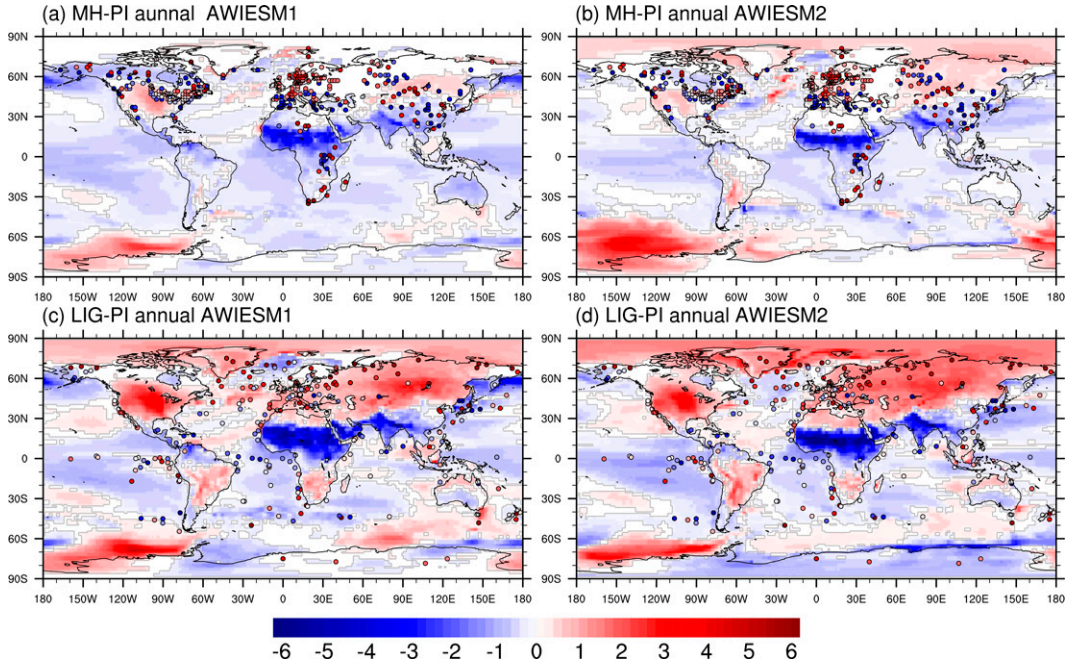

FIG. 3. Shading indicates simulated annual mean surface temperature anomalies (K) for (a) MH-PI in AWIESM1, (b) MH-PI in AWIESM2, (c) LIG-PI in AWIESM1, and (d) LIG-PI in AWIESM2. Only anomalies with significance levels larger than 95% based on Student's *t* test are shown. Circles indicate reconstruction of annual mean temperature anomalies for MH-PI (Bartlein et al. 2011) in (a) and (b) and LIG-PI (Turney and Jones 2010) in (c) and (d).

FESOM2.0 was built on the basis of the previous version (FESOM1.4) but is based on the finite-volume discretization (Danilov et al. 2017). It is also formulated on unstructured grids and offers multiresolution capabilities. The sea ice component in FESOM2.0 inherits the framework of FESOM1.4. FESOM2.0 uses the same 2D mesh and level surfaces as FESOM1.4, so the surface spatial resolutions used in the two model versions are the same. However, in the two model generations different vertical locations of main variables are applied (at layer surface in FESOM1.4, at layer center in FESOM2.0). Moreover, different transport schemes are used in FESOM1.4 (Taylor–Galerkin algorithm) and FESOM2.0 (mixture of the third-order upwind method and the fourth-order central differences). The 3D mesh of FESOM1.4 is generated by dropping vertical lines starting from the surface 2D nodes, forming prisms that are then cut into tetrahedral elements, while FESOM2.0 is discretized on prisms and formulated using the arbitrary Lagrangian Eulerian (ALE) vertical coordinate, which increases model flexibility. The same vertical mixing and eddy parameterizations as in FESOM1.4 are used in FESOM2.0. Compared to FESOM1.4, this new version improves the numerical efficiency in terms of computing time by at least 3 times while preserving its fidelity in simulating sea ice and the ocean (Scholz et al. 2019).

b. Experimental design

With each model, we perform three time-slice simulations for the PI, MH and LIG time periods. For the atmosphere, we initiate our simulations with the mean climatology obtained from an Atmospheric Model Intercomparison Project (AMIP) simulation, which has been conducted using prescribed sea surface temperatures and sea ice cover for 1978–99 (Roeckner et al. 2004). The initial state of the ocean is from the objectively analyzed climatological fields of temperature and salinity from the *World Ocean Atlas* (*WOA09*; https://www.nodc.noaa.gov/OC5/WOA09/pr_woa09.html), which represent the mean values from the 1950s through 2000s. Table 1 provides a summary of the boundary conditions following the protocols of PMIP4 (Otto-Bliesner et al. 2017). Orbital parameters are calculated following Berger (1977), and the greenhouse gas concentrations are taken from multiarchive reconstructions from the Greenland and the Antarctic ice cores (Flückiger et al. 2002; Monnin et al. 2004; Schneider et al. 2013; Schilt et al. 2010; Buiron et al. 2011). All experiments are configured on T63L47 grid for the atmosphere, with 47 levels in the vertical direction and a mean horizontal resolution of about 1.9° × 1.9°, which corresponds to a horizontal grid spacing of approximately 140 km × 210 km at midlatitudes. The ocean component applies a spatially variable resolution from about 100 km in the open ocean to 25 km over polar areas and 35 km along coastlines. A refined grid with a resolution up to 35 km is employed for the equatorial belt. In our simulations, the dynamic vegetation is interactively calculated via the land surface model JSBACH. Each simulation is integrated for 1000 model years with the trend of simulated global mean surface temperature in the final 100 model years not exceeding ± 0.05 K century^{-1}. Therefore, for each climate parameter, its average over the last 100 model years is considered to be representative of the climatology.

Unauthenticated | Downloaded 12/20/22 12:13 PM UTC

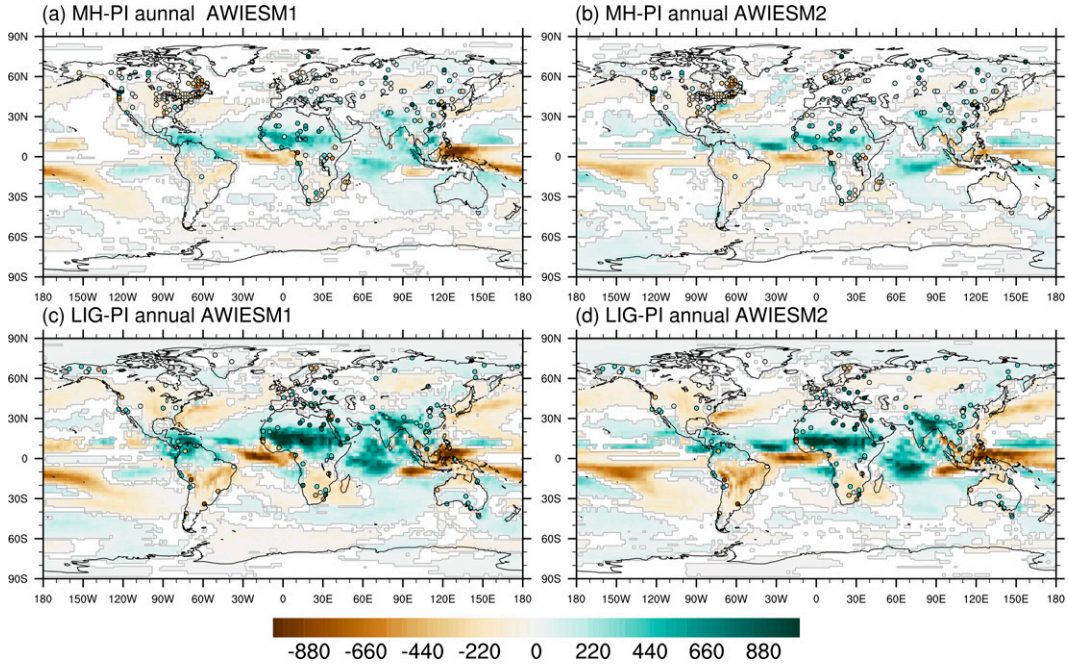

FIG. 4. Shading indicates simulated annual mean precipitation anomalies (mm yr^{-1}) for (a) MH-PI in AWIESM1, (b) MH-PI in AWIESM2, (c) LIG-PI in AWIESM1, and (d) LIG-PI in AWIESM2. Only anomalies with significance levels larger than 95% based on Student's *t* test are shown. Circles indicate reconstructed anomalies of annual mean precipitation between LIG and PI (Bartlein et al. 2011) in (a) and (b), and the same in (c) and (d) but on a semi-quantitative scale (see Scussolini et al. 2019): dark blue (much wetter), light blue (wetter), white (no noticeable anomaly), light red (drier), and dark red (much drier).

3. Results

a. Insolation and calendar option

Variations in Earth's orbital configuration lead to redistribution of the solar insolation across seasons and latitudes. When comparing seasonal changes between the past and present climates, artificial bias could be introduced by utilizing today's "fixed-day" calendar (Bartlein and Shafer 2019; Joussaume and Braconnot 1997; Shi et al. 2022). Due to changes in Earth's orbital elements, the insolation cycle is different today than it was in the past. As a result, the beginning and length of each month/season in the traditional fixed-day calendar are unlikely to match past insolation cycles.

Using today's fixed-day calendar, we display the insolation changes between the mid-Holocene and present as a function of latitude and time (month), shown in Fig. 1a. In comparison to PI, in MH there is more incoming solar insolation during boreal summer (autumn) over the Northern (Southern) Hemisphere high latitudes. Less energy is received between January and April, especially in the Southern Hemisphere. The above changes are similar but less pronounced under the angular calendar, as depicted in Fig. 1b. For LIG, however, the insolation changes between the classical mean and the angular mean is very evident (Figs. 1c,d): the decrease (increase) in solar insolation at high northern (southern) latitudes during boreal autumn is an artificial signal caused by the use of the classical calendar, which does not appear in angular means. Therefore, we converted the original classical calendar for each experiment to an angular calendar using the calendar adjustment method described in Shi et al. (2022).

In the following subsections we present the climate responses to changes in boundary conditions between the two warm interglacial and preindustrial periods simulated by AWIESM1 and AWIESM2. For each experiment, the seasonal and annual mean climatology is represented by the mean of the climate parameters over the last 100 model years. All of the findings of the present study are based on calendar-adjusted data.

b. Surface properties

Both models represent an enhanced Northern Hemisphere seasonality in both MH and LIG compared to PI, characterized by cooler northern winters and warmer northern summers (Fig. 2), with the anomalies being larger for LIG than for MH. This pattern is caused by changes in the Earth's orbital configuration, leading to a redistribution of seasonal and latitudinal solar insolation (Fig. 1). During the two interglacial periods, the Northern Hemisphere receives more incoming solar insolation at the top of the atmosphere in JJA and less in DJF than during the preindustrial era. In both interglacial simulations, temperature anomalies are greater over continents than over oceans. This striking contrast between land and sea is partly due to much larger heat capacity of the seawater compared to continents, implying that land surfaces heat up much faster. In addition, compared to land surfaces, oceans tend to release larger latent heat (Joshi et al. 2008).

Unauthenticated | Downloaded 12/20/22 12:13 PM UTC

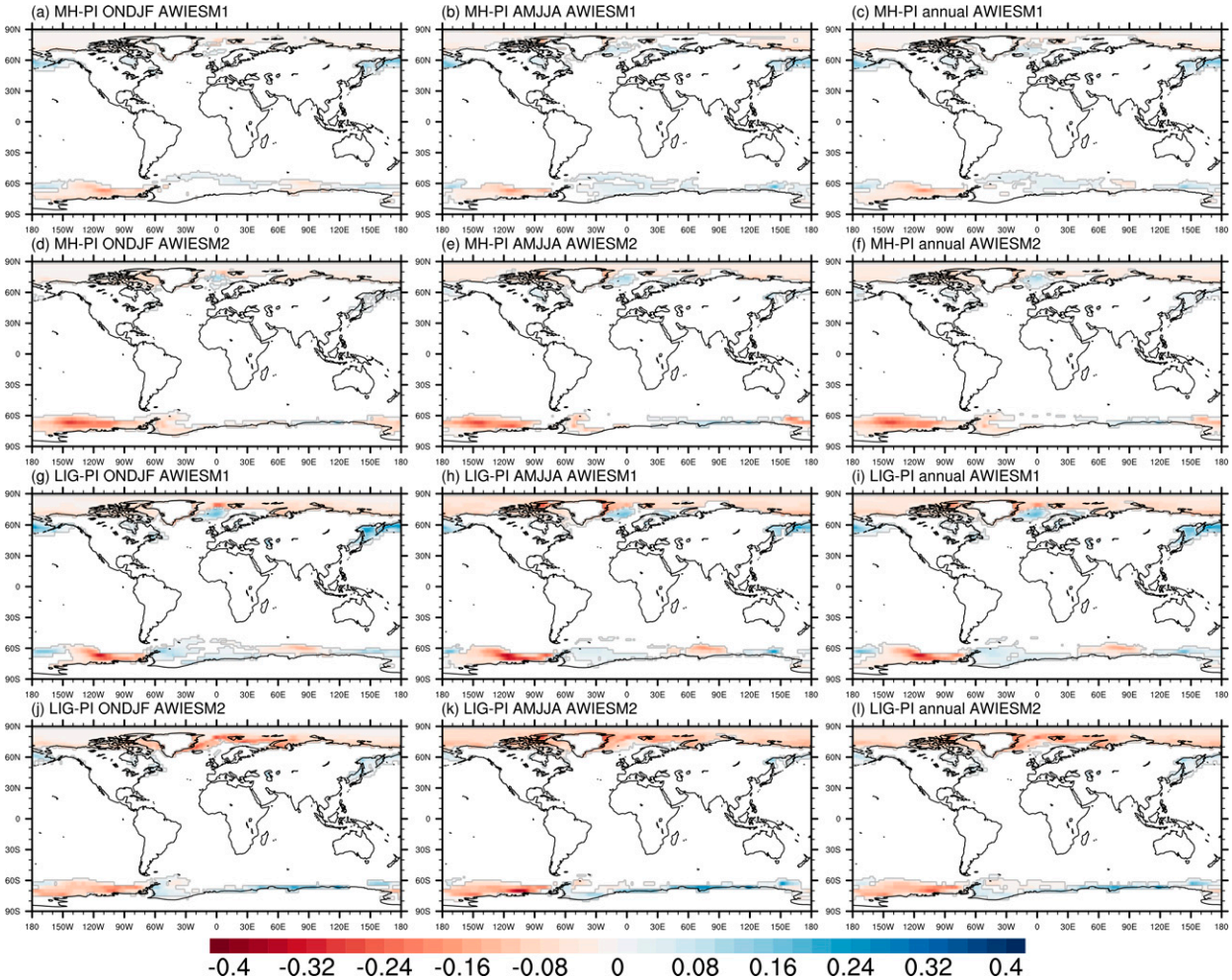

FIG. 5. Simulated anomalies of sea ice concentration between MH and PI for (a),(d) October–February (ONDJF), (b),(e) April–August (AMJJA), and (c),(f) the annual mean. (g)–(l) As in (a)–(f), but for sea ice concentration anomalies between LIG and PI. Only anomalies with significance levels larger than 95% based on Student's *t* test are shown.

Another intriguing feature is the cooling of the southern Sahara, which is associated with increased precipitation. The simulated LIG cooling of the Sahara and the warming of the Northern Hemisphere continents are more prominent in AWIESM2 than in AWIESM1. The pronounced LIG warming in DJF over the Arctic Ocean simulated by AWIESM2 is closely related to a reduction of sea ice, shown later in this paper. For the annual mean surface temperature during the mid-Holocene (Figs. 3a,b), slight positive anomalies are found over the Arctic and northern Eurasia, with an amplitude of less than 1 K, while the LIG annual mean temperature is dominated by a warming (up to 3 K) over the Arctic, Greenland, North America, and northern Eurasia, which is more pronounced in AWIESM2 than in AWIESM1 (Figs. 3c,d).

We assess our simulated annual mean surface temperature differences between the mid-Holocene and preindustrial periods using pollen-based continental temperature reconstructions compiled by Bartlein et al. (2011). We find spatial differences between model data and proxy data and between the two model generations. As depicted in Figs. 3a and 3b, the MH-minus-PI temperatures as indicated by the proxy data show general warming over western Europe, which is in line with our simulation results of AWIESM2, although with different magnitudes. In addition, both model versions are able to capture the dipole pattern of the temperature anomaly over eastern North America with cooling in the north and warming in the south. Our model results indicate a colder MH North Africa compared to PI, associated with an increased precipitation. This is in line with other PMIP4 models (Brierley et al. 2020) but opposite to the proxy, which shows a general warming over that region. The annual warming recorded by proxy is dominated by the summer signal: compared to PI, the earlier onset of the growing season and increase in insolation during the MH together result in a warming over Africa (Bartlein et al. 2011). As documented by the pollen proxy, Asia is characterized by a mix of positive and negative temperature anomalies between MH and PI, while both model versions show increased temperatures over

Unauthenticated | Downloaded 12/20/22 12:13 PM UTC

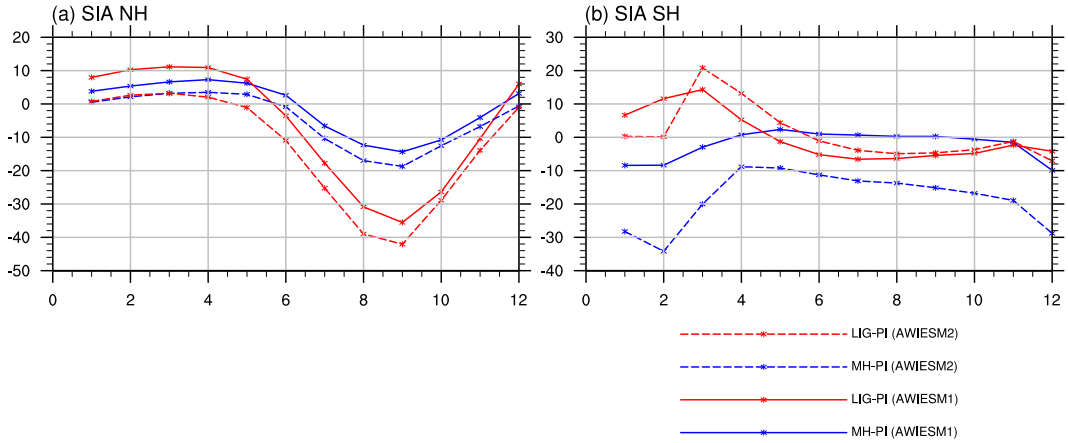

FIG. 6. The seasonal changes of sea ice area (SIA; %) in MH (blue lines) and LIG (red lines) relative to preindustrial in percentage. Solid lines represent results from AWIESM1, and dashed lines from AWIESM2.

northern Asia and decreased temperatures over southern Asia. Such a model–data mismatch is likely due to changes in local atmospheric circulations that tend to overwhelm the insolation effect (Bartlein et al. 2011). Moreover, we bear in mind that in many locations the pollen-based proxy record has a high degree of uncertainty (Bartlein et al. 2011).

The modeled LIG annual mean surface temperature anomalies relative to PI are evaluated against a global dataset comprising 263 published ice, marine, and terrestrial sequences spanning the LIG (Turney and Jones 2010). As seen in Figs. 3c and 3d, both model versions show a good agreement with the Northern Hemisphere warming registered in geologic records, with the exception of the Nordic seas in AWIESM1 and the North Atlantic in AWIESM2. Both proxy and model simulations point to a general cooling over tropical oceans and northern Africa. AWIESM1 is even able to capture localized warming over the eastern Pacific. However, the warming of Antarctic as revealed in proxy data is not detected in our models. One thing to be noted here is that according to the protocol of PMIP4 described in Otto-Bliesner et al. (2017), the ice sheet orography in LIG simulations is kept the same as in PI. However, sea level reconstructions based on fossil corals indicate a global mean sea level rise of about 7.6 m during the LIG than at present, with the Antarctic ice sheet being the most significant source of meltwater (Dutton et al. 2015). This lack of implementation of Antarctic topographical changes may explain our model–data discrepancy for the surface temperature over the Antarctic.

Changes in annual mean precipitation are shown in Fig. 4. The most prominent feature is the increased rainfall in the North Africa monsoon region (5°–23.3°N, 15°W–30°E) during the mid-Holocene and the last interglacial, which is more profound in AWIESM1 than in AWIESM2. Moreover, wetter conditions are also found in other Northern Hemisphere monsoon domains, namely North America (5°–30°N, 100°–40°W) and South Asia (5°–23.3°N, 70°W–120°E), associated with a northward displacement of the ITCZ. Pollen-based precipitation records compiled by Bartlein et al. (2011) are used to validate the simulated precipitation anomalies between MH and PI. Wetter conditions are documented by proxy records over the southern Sahara and South Asia, in good agreement with our simulation results for both the sign and magnitude. Over Eurasia, some proxy records suggest much wetter conditions in MH than in PI, but they can also be an indication of very localized precipitation. For the northern Sahara, our models largely underestimate the increase in precipitation between MH and PI. Another striking feature displayed by proxy records is the dryness over eastern North America (up to -400 mm yr^{-1}), while both model versions do not show apparent changes in precipitation. Such discrepancy may arise from model biases, but can also be related to reconstruction biases. We evaluate the simulated LIG-minus-PI precipitation against a recent proxy database compiled by Scussolini et al. (2019). A wetter LIG over most parts of the global continents is shown by the various proxy records, with dryness occurring in some regions such as the southern part of South America, northern Europe, and western Australia. Our modeled results are generally in line with the proxy, showing that the largest precipitation anomaly between LIG and present-day happens in the Northern Hemisphere tropics, but both models underestimate the wettening in Africa and central Europe. Overall, our results regarding the MH-minus-PI and LIG-minus-PI surface temperature and precipitation for AWIESM1 and AWIESM2 agree well with other PMIP4 models (Brierley et al. 2020; Otto-Bliesner et al. 2021).

Sea ice concentration (SIC) is strongly coupled with changes in surface temperature. During melting months of the Arctic [April–August (AMJJA)], warming of the Arctic Ocean gives rise to an overall reduction in sea ice coverage for both interglacial periods (Fig. 5). This change is more pronounced in LIG than in MH, and more evident in AWIESM2 than in AWIESM1. During freezing seasons of the Northern Hemisphere [October–February (ONDJF)], despite the reduced insolation, negative anomalies of the sea ice concentrations are observed in both MH and LIG for the Arctic Ocean, as less sea ice has been accumulated during the previous freezing months. Generally, we see a decline in Arctic annual mean sea ice concentration during MH and LIG relative to

Unauthenticated | Downloaded 12/20/22 12:13 PM UTC

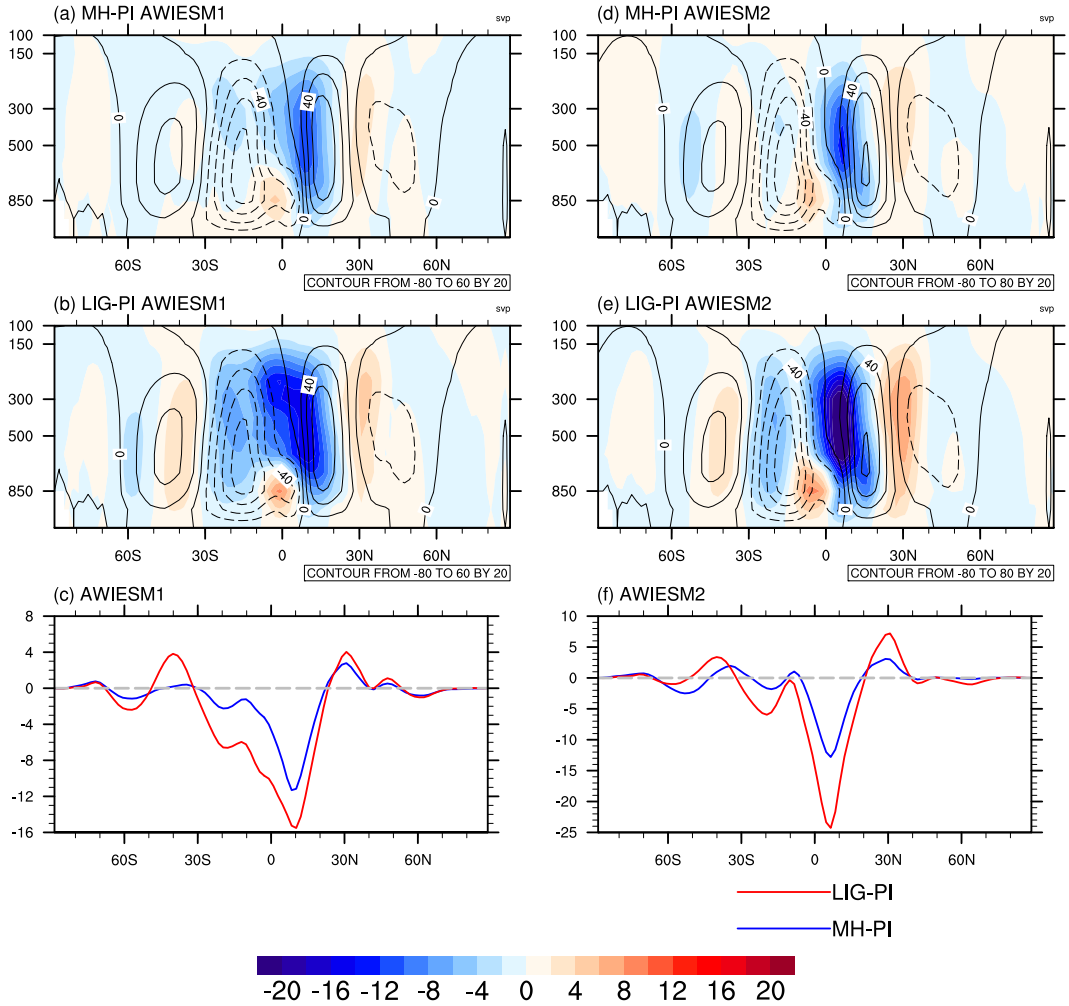

FIG. 7. Simulated anomalies of zonal-mean meridional streamfunction (svp; 1 svp = 10^9 kg s^{-1}) for (a) MH minus PI in AWIESM1 and (b) LIG minus PI in AWIESM1. (c) The anomaly of meridional streamfunction at 500-hPa pressure level for MH-PI (blue) and LIG-PI (red), as simulated by AWIESM1. (d)–(f) As in (a)–(c), but for AWIESM2.

PI. In comparison to preindustrial times, the western Southern Ocean experiences a warming during the two interglacial periods, resulting in a reduction in sea ice concentration all year round.

Here, we show seasonal anomalies in the sea ice area (SIA) between interglacial and preindustrial time periods. To define the SIA, we first calculate the sea ice area for each grid cell, which is simply the product of the sea ice concentration and the area of the corresponding ocean cell, and then we sum the sea ice area across all grid cells over the Northern or Southern Hemisphere. The result is shown in Fig. 6. Both model versions reveal an increase in mid-Holocene SIA over the Arctic Ocean from January to May, with a larger difference in AWIESM1 than in AWIESM2. In December and June, AWIESM1 presents positive anomalies in the Arctic SIA between MH and PI, while AWIESM2 shows the opposite results. From July to November, both models simulate a decrease in Arctic SIA during MH, and this change is greater in AWIESM2 than in AWIESM1. Similarly, the Northern Hemisphere SIA during the LIG also shows an enhancement in its seasonality compared to PI, with an increase in SIA in boreal winter and a decrease in boreal summer, associated with the increased seasonality in solar insolation and surface air temperature. The largest reduction in Northern Hemisphere SIA occurs in September, with the anomaly percentage being greater than −35% for both models.

Regarding the SIA anomalies between MH and PI for the Southern Hemisphere, we observe a discrepancy between the two model versions. From April to November, no obvious change in MH SIA is noted in AWIESM1, while a significant reduction of MH SIA is presented in AWIESM2. The former is due to a compensation of deceased sea ice cover in the Bellingshausen Sea and increased sea ice concentration over other parts of the Southern Ocean (Fig. 5b). In contrast, in AWIESM2, the sea ice reduction in the Bellingshausen Sea is pronounced and dominates an overall decrease in Southern Hemisphere SIA (Fig. 5e). A common feature shared by both models is a decline in the MH SIA from December to March,

Unauthenticated | Downloaded 12/20/22 12:13 PM UTC

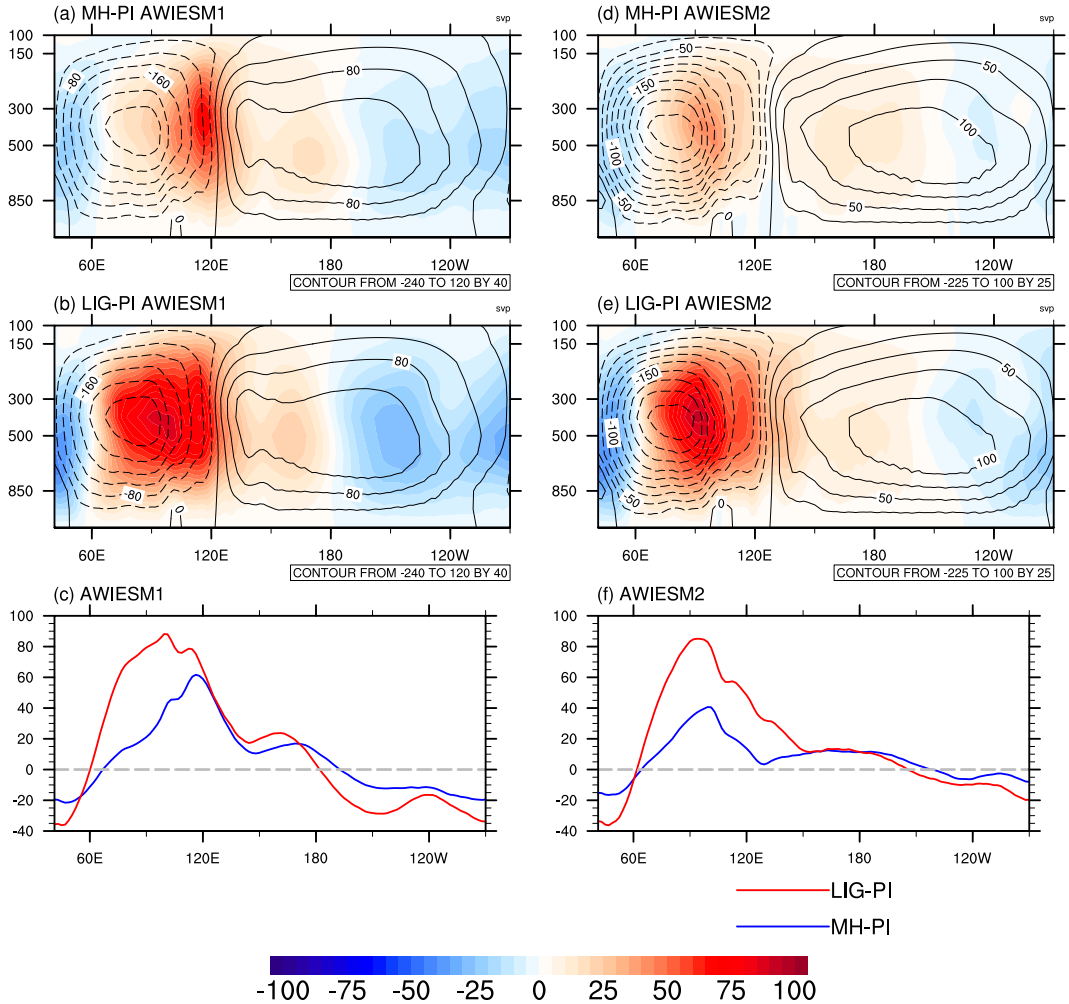

FIG. 8. Simulated anomalies of zonal mass streamfunction (svp) over 10°S–10°N, 40°E–90°W for (a) MH minus PI in AWIESM1 and (b) LIG minus PI in AWIESM1. (c) The anomaly of zonal mass streamfunction at 500-hPa pressure level for MH-PI (blue) and LIG-PI (red), as simulated by AWIESM1. (d)–(f) As in (a)–(c), but for AWIESM2.

which is more profound in AWIESM2 than in AWIESM1. Both models agree that the SIA in the Southern Ocean decreases during the LIG period compared to PI from June to December. In AWIESM2, no apparent change in LIG SIA is found for January and February, while the SIA simulated by AWIESM1 has a positive anomaly. Both models show increased LIG SIA in April and decreased values in December relative to PI. Furthermore, for AWIESM1, we find that the responses of Southern Hemisphere SIA are very different for MH and LIG especially during austral summer. This is because the warming at the Bellingshausen Sea (Fig. 2a) during MH simulated by AWIESM1 drives a decline in sea ice. A similar pattern can be seen in LIG but the SIA anomaly between LIG and PI is overwhelmed by the increased sea ice cover in the Weddell Sea, led by the cooling in that region (Fig. 2g).

c. *Large-scale atmospheric circulation*

The Hadley circulation is characterized by ascending motion in the tropics and descending motion in the subtropical regions. As previous studies have revealed, the intensity of the Hadley circulation is primarily determined by the

TABLE 2. Walker circulation index as defined by U_{850} (m s^{-1}).

	PWC (AWIESM1)	PWC (AWIESM2)	IWC (AWIESM1)	IWC (AWIESM2)
PI	−7.66	−6.56	2.76	2.21
MH	−8.01	−6.98	2.60	1.91
LIG	−7.89	−7.36	1.76	1.35

Unauthenticated | Downloaded 12/20/22 12:13 PM UTC

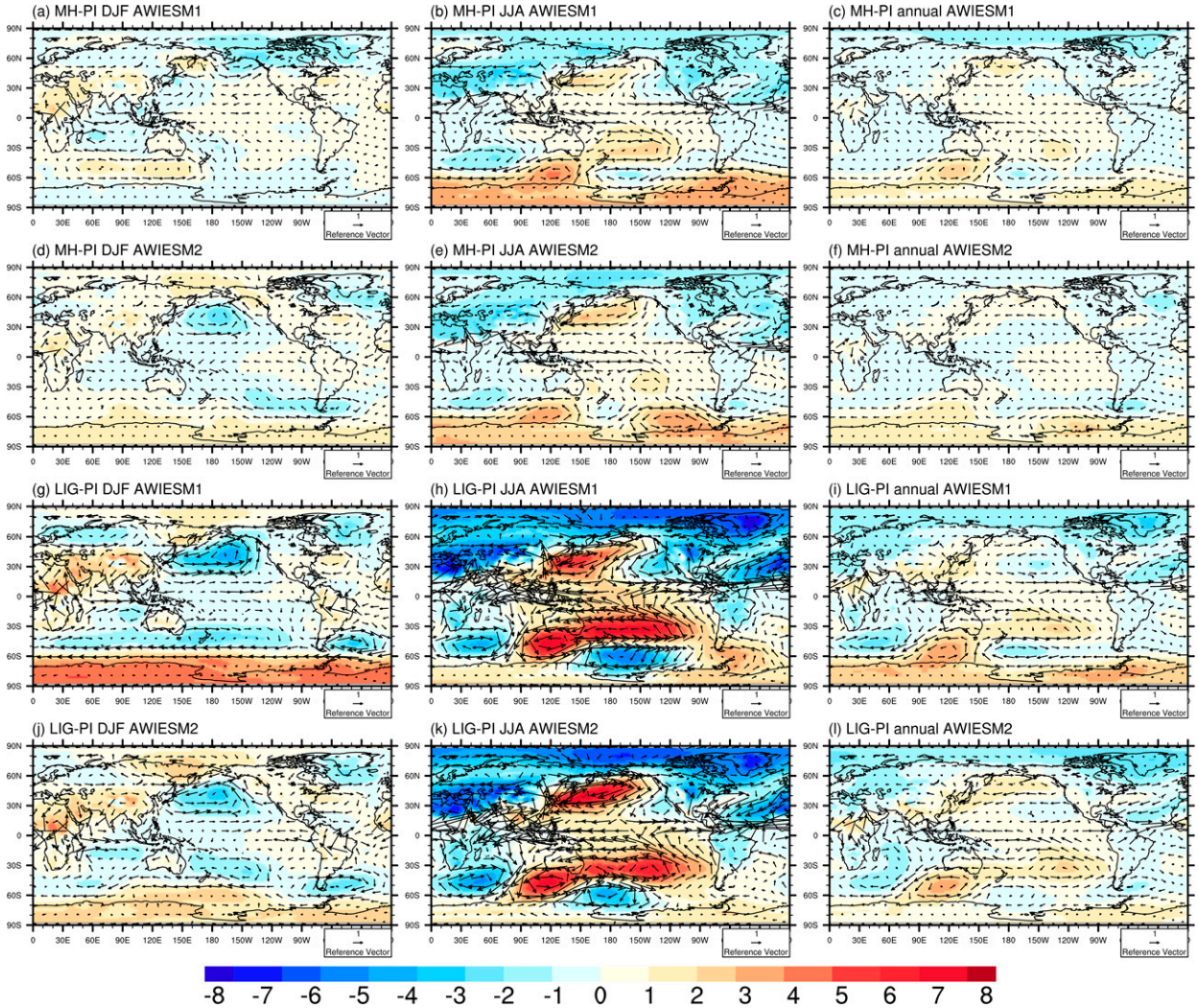

FIG. 9. Simulated anomalies of sea level pressure (shading; hPa) and 850-hPa wind (vector; m s^{-1}) between MH and PI for (a),(d) DJF, (b),(e) JJA, and (c),(f) the annual mean. (g)–(l) As in (a)–(f), but for anomalies between LIG and PI.

subtropical-to-equator temperature gradient (Yang et al. 2020a). Compared to the preindustrial period, the increase in annual mean surface temperature over the mid-to-high latitudes of the Northern Hemisphere during MH leads to a decrease in meridional temperature gradient, which favors a weakening in the Northern Hemisphere Hadley circulation (Fig. 7). We observe a similar and more pronounced response of the Hadley circulation to the LIG boundary conditions, as during LIG the change of the Northern Hemisphere thermal contrast is much greater than that during MH (Fig. 2). Moreover, we find that the anomalies in Northern Hemisphere Hadley circulation between the last interglacial and preindustrial time intervals are more evident in AWIESM2 than in AWIESM1. This can be explained by the greater warming in LIG over North America and Eurasia as simulated in AWIESM2 than in AWIESM1 (Fig. 2). For the Southern Hemisphere, although there is no apparent change in the subtropical-to-tropical surface temperature contrast in MH and LIG compared to PI (Fig. 2), we observe a slightly strengthened Hadley circulation. This strengthened Southern Hemisphere Hadley circulation is likely driven by stronger meridional insolation gradients, in particular at low latitudes during the LIG, as revealed in Fig. 1. We also notice a positive anomaly in the meridional streamfunction at the low-level region near the equator, which is due to the reduced temperature gradient caused by the Saharan cooling (Fig. 2). This effect is more prominent in LIG than in MH. In addition, there is an overall northward shift of the Hadley cell in the warm episodes with respect to the preindustrial, as indicated by the profile of anomalous meridional mass streamfunction at 500 hPa (Figs. 7c,f), which is closely related to the northward shift of the ITCZ.

The Pacific Walker circulation features rising air motion over the western Pacific, subsidence over the eastern Pacific, low-level easterlies across the central equatorial Pacific, and returning westerlies in the upper troposphere (300–100 hPa).

Unauthenticated | Downloaded 12/20/22 12:13 PM UTC

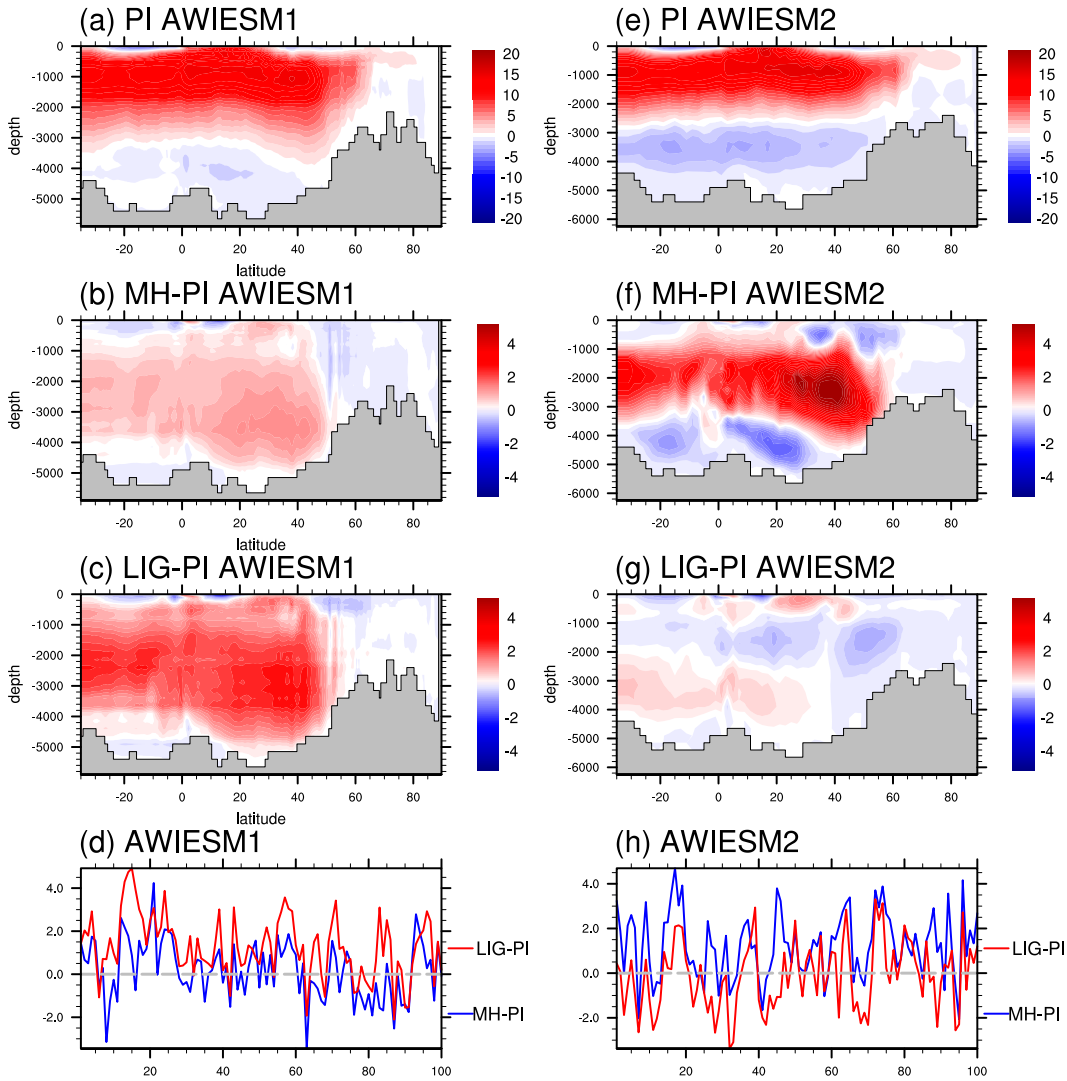

FIG. 10. Simulated streamfunction of zonally integrated meridional overturning circulation (Sv) over the Atlantic basin based on AWIESM1 for (a) PI, (b) MH minus PI, and (c) LIG minus PI. (d) AMOC index as simulated by AWIESM1 for MH-PI (blue) and LIG-PI (red). (e)–(h) As in (a)–(d), but from AWIESM2.

There are similar circulation cells covering various longitudinal bands across the equator, such as the circulation cells above Indian Ocean and Atlantic section. Today, the term "Walker circulation" generally refers to the totality of these circulation cells (Lau and Yang 2003). In the present study, we examine the main Walker circulation cell along the equatorial Pacific plane [hereafter referred to as Pacific Walker cell (PWC)], plus a secondary circulation cell above the Indian Ocean whose ascending air motion occurs over western Pacific with compensating subsidence over the Arabian Sea [hereafter referred to as Indian Walker cell (IWC)]. The contours depicted in Fig. 8 representing the simulated preindustrial zonal mass streamfunction (calculated based on divergent component of the wind) averaged over the Indo-Pacific region (10°S–10°N, 40°E–90°W) show a good agreement with previous studies (Zhang et al. 2021; Lau and Yang 2003). Relative to the preindustrial period, both interglacial episodes show an intensification and a westward shift of the ascension over the tropical western Pacific, indicating a westward displacement of both the Pacific and Indian Walker cells. One exception is the mid-Holocene pattern as simulated by AWIESM2 (Fig. 8d), which shows no clear shift. Similar conclusions can also be drawn from Figs. 8c and 8f. With respect to PI, the zonal mass streamfunction over Pacific sector shows positive anomalies on the west side and negative anomalies on the east side of the cell during MH and LIG in both model versions, resulting from the westward shift of the Walker circulation.

To indirectly represent the strength of the atmospheric circulation for PWC, here we use the indices defined by the average 850-hPa zonal wind (U_{850}) in the equatorial Pacific (i.e., 5°S–5°N, 130°E–100°W), following Tian et al. (2018). A

Unauthenticated | Downloaded 12/20/22 12:13 PM UTC

TABLE 3. AMOC strengths (maximum value within 800–2000 m and 20°–90°N) in each simulation, and anomalies between MH/LIG and PI. Anomaly values with a significance level larger than 95% (based on Student's *t* test) are written in bold. Units are Sverdrups.

	PI	MH	LIG	MH − PI	LIG − PI
AWIESM1	15.5	15.7	16.8	0.2	**1.3**
AWIESM2	16.3	17.5	16.2	**1.2**	−0.1

similar index measuring the surface flow of IWC is calculated as the average of U_{850} over the equatorial Indian Ocean (5°S–5°N, 40°–100°E). There is a strengthening of the PWC during both interglacial periods compared to the present in both models, indicated by the increase in easterly winds as illustrated in Table 2. In addition, the low-level westerly belt over the tropical Indian Ocean decreases during the two warm episodes with respect to PI, again revealing a weakening of the Indian Walker cell.

We observe a large seasonal difference of the U_{850} change over the equatorial belt between the interglacial and preindustrial periods. As depicted in Fig. 9, relative to PI, both models show anomalous westerly winds over the equatorial Indian Ocean and western equatorial Pacific during boreal winter, while the opposite signals during boreal summer with pronounced easterly and westerly winds over 40°E–150°W and 140°–100°W are revealed, respectively. Overall, the annual mean U_{850} changes are dominated by the boreal summer anomalies, which are partially offset by the boreal winter anomalies, resulting in an enhancement in the annual mean PWC and a decline of the annual mean IWC. Therefore, the changes of both Walker circulation cells are mainly contributed by the JJA-anomaly pattern.

From a climatological perspective, the Walker circulation is maintained by zonal temperature gradients, with the ascending branch occurring over the western Pacific warm pool (Cornejo-Garrido and Stone 1977; Chervin and Druyan 1984; Lau and Yang 2003; Kang et al. 2020). Due to the uneven land–sea distribution, increasing boreal summer insolation during the MH and LIG introduces more pronounced surface warming over the Eurasian and North Africa than over oceans (Figs. 2b,e,h,k), causing a westward shift of the Indo-Pacific Walker circulation. Additionally, the uneven temperature changes increase (decrease) the zonal temperature gradient at the Pacific (Indian) Ocean sectors. As a consequence, anomalous easterly winds are observed over the western Pacific and Indian Ocean, resulting in

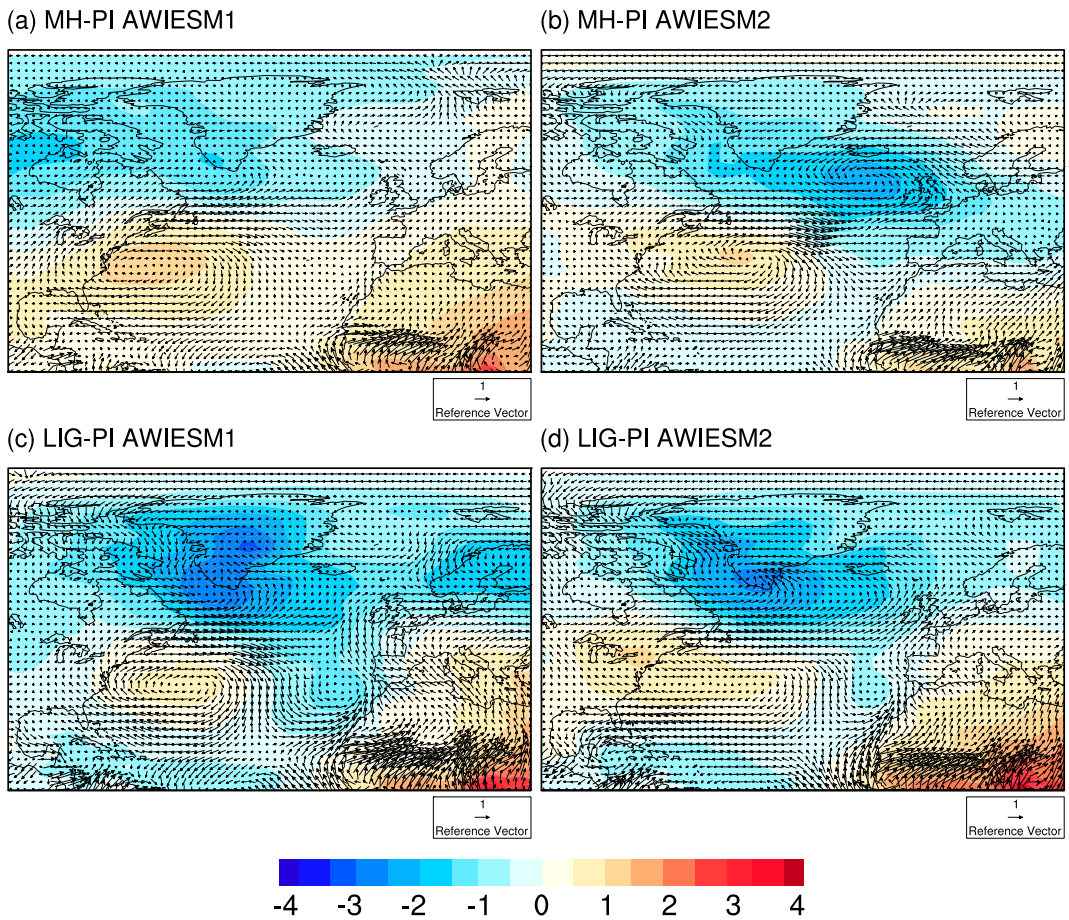

FIG. 11. Simulated anomalies of SLP (shading; hPa) and low-level winds (vector; m s^{-1}) over the North Atlantic region.

Unauthenticated | Downloaded 12/20/22 12:13 PM UTC

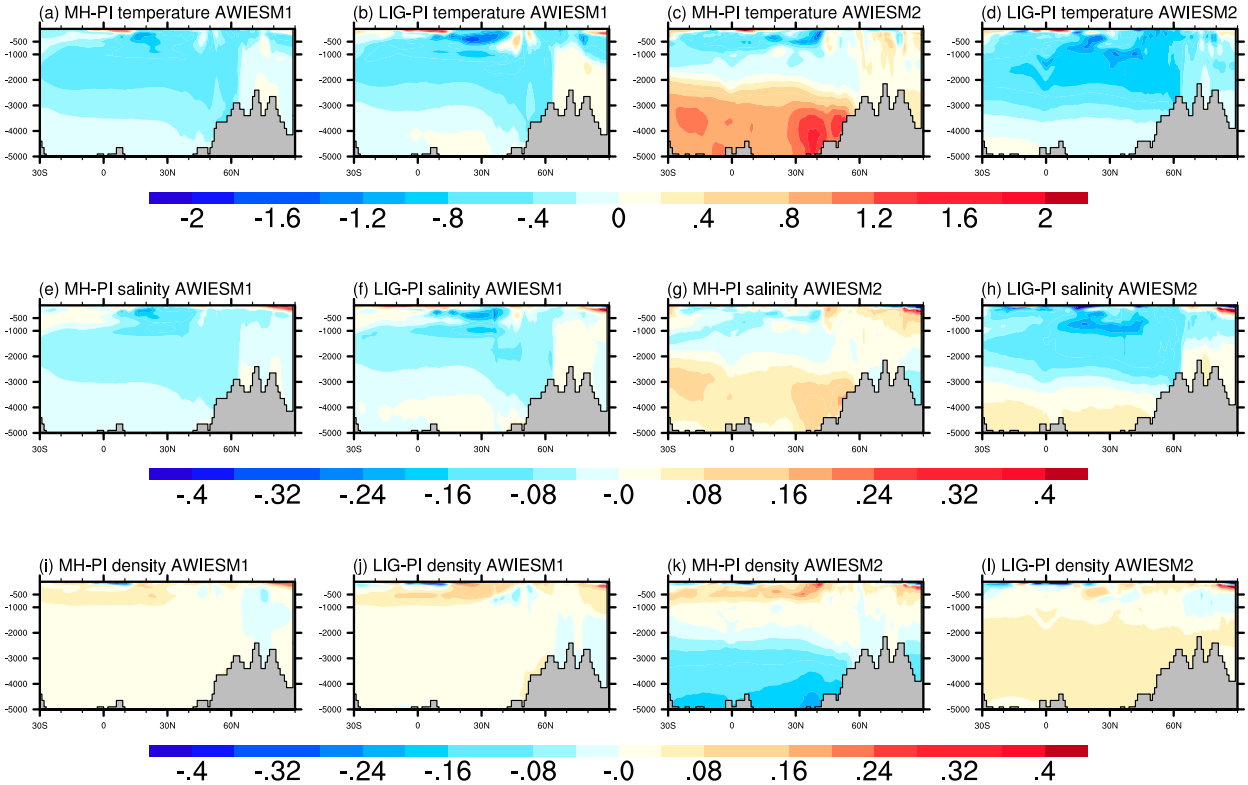

FIG. 12. Simulated zonal mean anomalies over the North Atlantic sector for (a)–(d) ocean temperature (K), (e)–(h) ocean salinity (psu), and (i)–(l) ocean density (kg m^{-3}).

strengthening of the Pacific Walker cell and weakening of the Indian Walker cell.

Similar results regarding the response of the Indo-Pacific Walker circulation to interglacial boundary conditions are found in previous studies (Tian et al. 2018; Chang and Li 2000). They attribute such a change to the summer monsoon system in South Asia and North Africa. Their studies suggest that the enhanced convective heating in the monsoon regions, led by increased summer monsoon precipitation, is beneficial to anomalous easterly winds at the equatorial plane over western Pacific and Indian Ocean through a Kelvin wave response, resulting in a strengthening of the Pacific Walker cell and a weakening of the Indian Walker cell.

d. *Large-scale oceanic circulation*

The Atlantic meridional overturning circulation (AMOC) can be characterized by the zonally integrated streamfunction over the Atlantic basin, and the AMOC strength is calculated as the maximum value of AMOC within the depths of 800–2000 m, and between 20° and 90°N in the Atlantic. The simulated preindustrial AMOC index is 15.5 Sv (1 Sv ≡ 10^6 m^3 s^{-1}) and 16.3 Sv in AWIESM1 and AWIESM2 (Fig. 10), respectively, both agree with the estimated value based on the hydrographic data from World Ocean Circulation Experiment (WOCE) (Ganachaud and Wunsch 2000), but slightly lower than the values suggested by Talley (2013) and Frajka-Williams et al. (2019). In the mid-Holocene experiments, the AMOC strength increases by 1.2 Sv in AWIESM2 compared to the preindustrial, while in AWIESM1 the anomaly is only 0.2 Sv, much lower than the standard deviation of AMOC strength (i.e., about 1 Sv). Comparing different model versions, opposite AMOC anomalies between LIG and PI are simulated as shown in Figs. 10c and 10g: AWIESM1 reproduces a strengthening in LIG AMOC with a magnitude of about 1.3 Sv compared to PI. In contrast, AWIESM2 presents a slight and nonrobust decrease by 0.1 Sv in the LIG-minus-PI AMOC strength (see also Table 3).

The response of AMOC is associated with the change in background atmospheric circulation over the North Atlantic Ocean. The changes in SLP, as shown in Fig. 11, indicate an anomalous positive mode of the North Atlantic Oscillation (NAO) during boreal winter in MH and LIG compared to PI, as simulated by both models. Common features in the interglacial experiments include an anomalous negative SLP north of 50°N, a positive SLP anomaly south of 50°N centering at western North Atlantic, and a tendency toward an enhanced latitudinal SLP gradient (i.e., positive NAO-like phase). The wind anomaly is characterized by an increased westerly over the North Atlantic subpolar regions, which helps to strengthen the deep water formation (Köhl 2005; Eden and Willebrand 2001; Latif et al. 2006; Scholz et al. 2014).

The changes in SLP and surface winds over the North Atlantic cannot fully explain the response of AMOC to MH and LIG boundary conditions in the two model versions. Here we turn to examine the zonal mean temperature, salinity, and

Unauthenticated | Downloaded 12/20/22 12:13 PM UTC

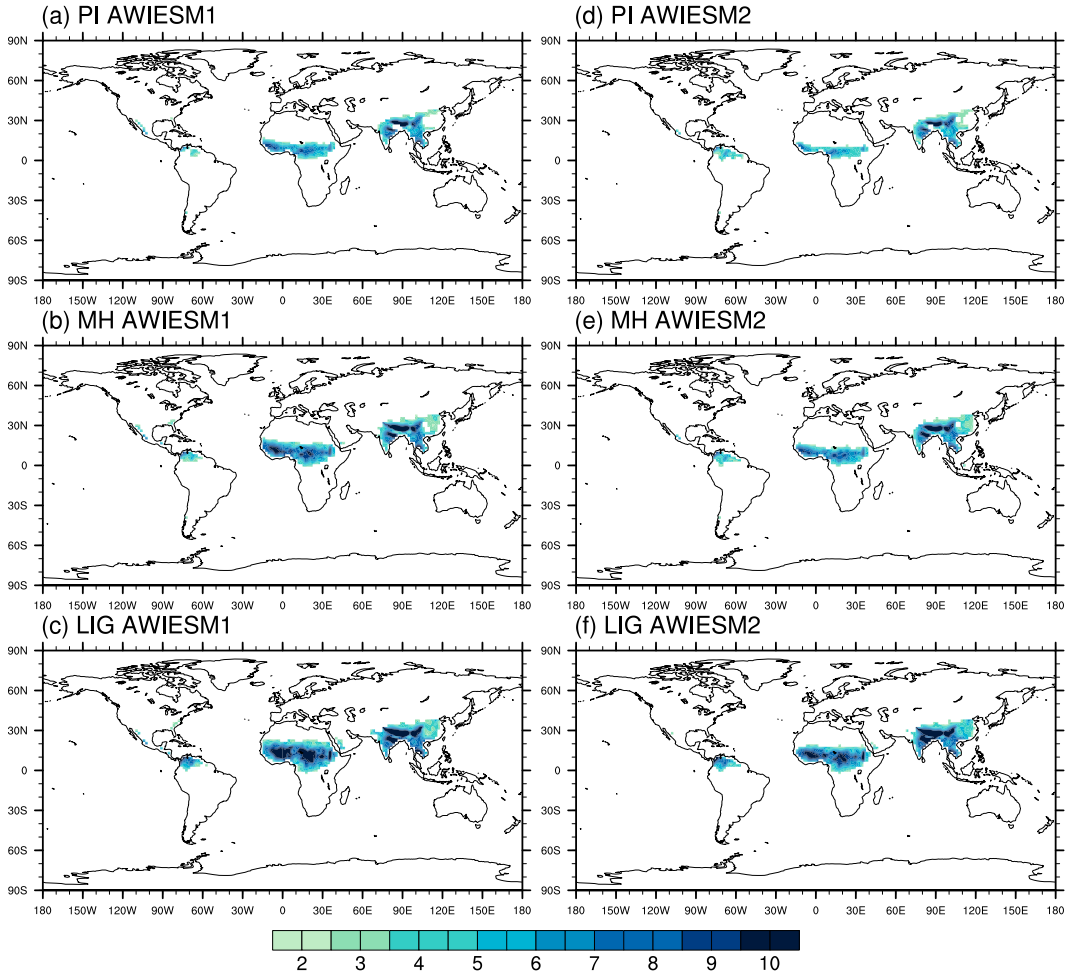

FIG. 13. Monsoon domains and precipitation changes (mm day^{-1}) between JJAS and DJFM for (a),(d) PI, (b),(e) MH, and (c),(f) LIG, based on (left) AWIESM1 and (right) AWIESM2.

density of the ocean across the Atlantic sector. As shown in Fig. 12, in AWIESM1 we observe cooling and freshening in the MH and LIG seawater above 3000 m, which is more profound in LIG than in MH. The positive density anomalies of the upper ocean in 0°–40°N (Figs. 12i,j) are a consequence of the cooling. This increases the instability of the seawater column. In contrast, we find very different results related to AWIESM2 simulations: MH is represented with heavier seawater in the upper layers and lighter seawater in the deep and bottom ocean (Fig. 12k), with the former driven through the surface cooling shown in Fig. 12c and the latter led by the pronounced warming of seawater below 3000 m (Fig. 12c). Such a pattern of density changes contributes to a strengthening of deep water formation over the North Atlantic and a deepening of the North Atlantic Deep Water (NADW). The LIG simulated by AWIESM2 reveals a general increase in seawater density below 2000 m (Fig. 12l), which is due to cooling in deep layers (Fig. 12d) as well as to the salinification in bottom layers (Fig. 12h). The increase in the density gradient between the upper and deep ocean gives rise to an enhancement in ocean stability.

Thus, we conclude that the complex AMOC responses shown in Fig. 10 are affected by both the atmospheric changes and the changes in oceanic properties (Fig. 12). Moreover, we are aware of that the AMOC changes in MH simulated by AWIESM1 and in LIG simulated by AWIESM2 are small and do not exceed the standard deviation of the AMOC strength (approximately 1 Sv).

The two model versions yield different AMOC responses to MH and LIG boundary conditions, which could be due to different numerical schemes employed in the ocean components (the two model versions have fully different dynamical cores). Our result could provide important information for understanding intermodel AMOC differences in PMIP. However, it should be noted that there are other minor updates between FESOM1 and FESOM2, such as the implementation details of the Gent–McWilliams (GM) thickness diffusivity, that could also have a potential to influence the simulated AMOC changes.

e. Monsoon

In this section we focus on the responses of Northern Hemisphere summer monsoon to MH and LIG climate states.

Unauthenticated | Downloaded 12/20/22 12:13 PM UTC

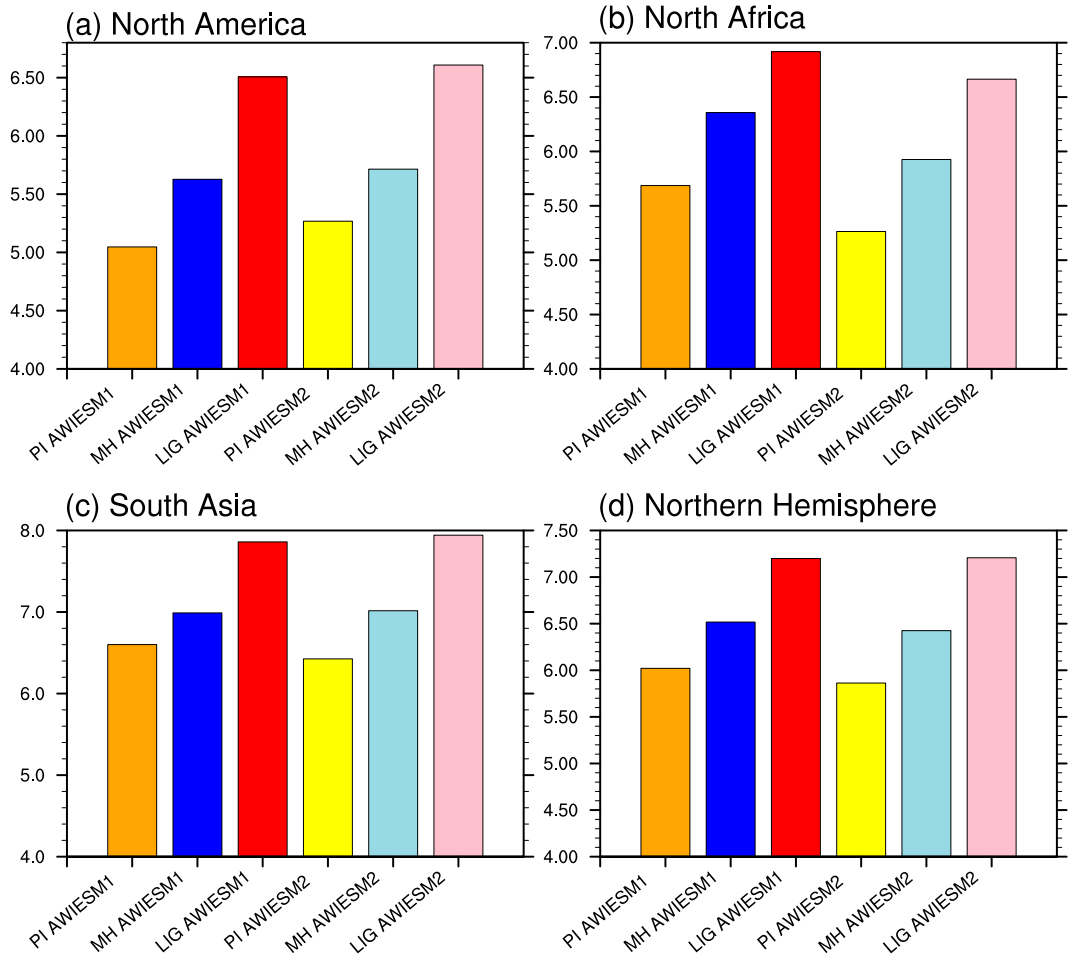

FIG. 14. Monsoon intensity (mm day^{-1}) for (a) North America, (b) North Africa, (c) South Asia, and (d) Northern Hemisphere.

We start with the experimentally simulated monsoon domain, which is defined as the area with the precipitation anomaly between JJAS (from June to September) and DJFM (from December to March) being larger than 2 mm day^{-1}, following D'Agostino et al. (2019). As depicted in Fig. 13, both models suggest that the area of each Northern Hemisphere monsoon region (i.e., North America, North Africa, and South Asia) is larger in MH than in PI. In comparison to MH and PI, the LIG experiences a northward expansion of Northern Hemisphere summer monsoon domains, especially for North Africa. Another intriguing feature is the enhanced seasonality of precipitation, defined as precipitation anomalies between JJAS and DJFM, over the three monsoon regions in interglacial relative to preindustrial time periods, which is more pronounced in LIG than in MH.

The intensity of monsoon rainfall is calculated as the JJAS-mean precipitation averaged over the respective Northern Hemisphere summer monsoon domain. As shown in Fig. 14, the intensities of MH and LIG summer monsoon rainfall increase relative to PI over all monsoon regions of the Northern Hemisphere, simulated by both models, and the differences are larger in LIG than in MH. Change in monsoon rainfall intensity can be contributed by a combination of both thermodynamic and dynamic factors: changes in specific humidity, which is the thermodynamic term, and changes in moisture flux convergence by the mean flow representing the dynamic component. Here, for each monsoon domain, we perform a decomposition analysis on the moisture budget in the thermodynamic and dynamic contributions following the method described in D'Agostino et al. (2019). Our results, as illustrated in Fig. 15, suggest that the dynamic component, primarily associated with changes in background atmospheric mean flow, largely determines the responses of Northern Hemisphere continental monsoonal precipitation. In contrast, the thermodynamic component tends to cause negative anomalies of monsoonal rainfall over South Asia and, more evidently, over North America.

The dynamic component is closely related to net energy input (NEI) of the atmosphere which is defined as the difference between the net radiative flux received at the top of the atmosphere and the total energy fluxes received at the surface. During the interglacial warm episodes, insolation changes lead to

Unauthenticated | Downloaded 12/20/22 12:13 PM UTC

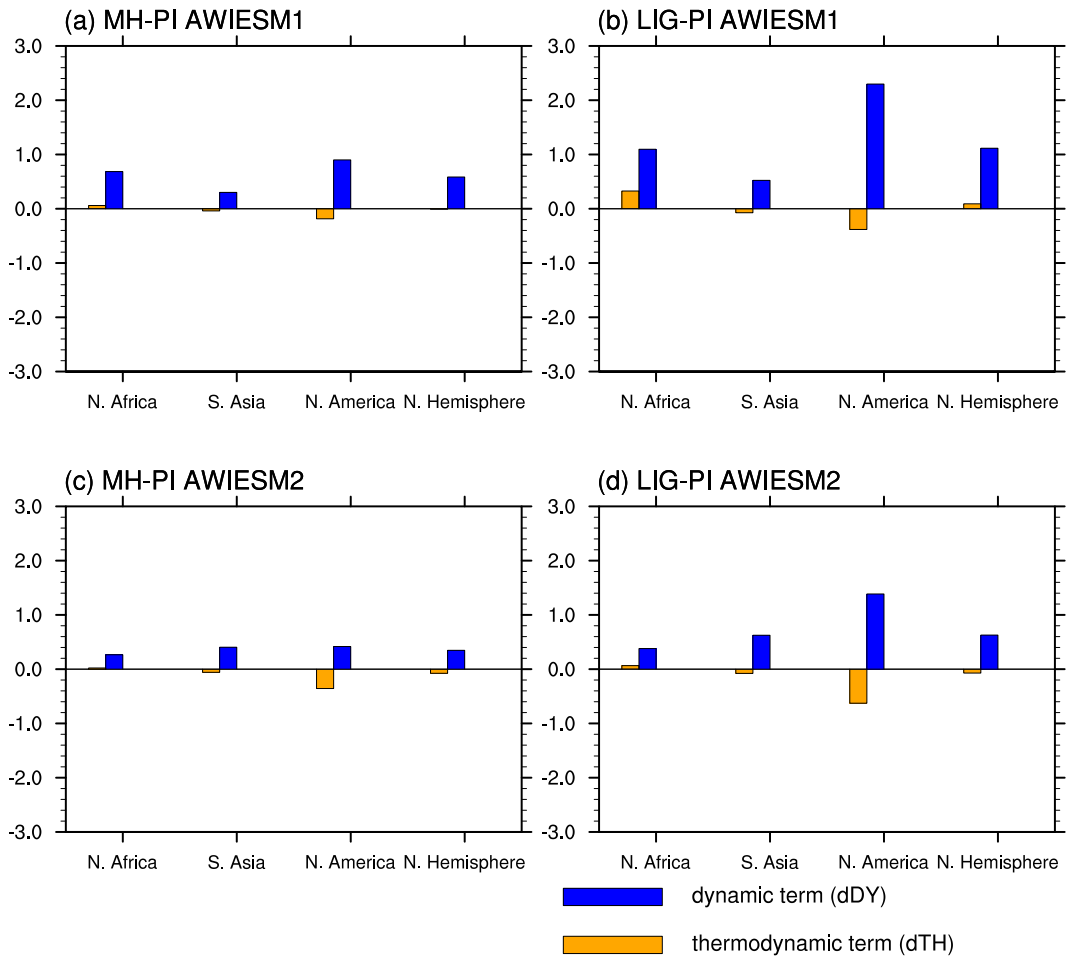

FIG. 15. Decomposition analysis for monsoon moisture budget (mm day^{-1}). Blue bars represent the contribution from the dynamic term and orange for the thermodynamic component.

more NEI over Northern Hemisphere continents during the warm months. This anomalous positive net energy input, according to Chou et al. (2001), Boos and Korty (2016), Merlis et al. (2013), and D'Agostino et al. (2019), is compensated by anomalous meridional energy transport, implying a strengthening in atmospheric monsoonal circulation during boreal summer.

4. Summary and conclusions

The present study documents the results from three PMIP4 simulations, including a preindustrial control simulation and two interglacial runs for the mid-Holocene and last interglacial period, conducted with two generations of AWI-ESM. The boundary conditions prescribed in each experiment (i.e., orbital parameters and greenhouse gas concentrations), are configured according to the protocol of PMIP4. Our study focuses on the differences of large-scale properties of Earth's surface, the atmosphere, and the ocean between relatively warm interglacial episodes and the preindustrial era.

In comparison with the preindustrial, our interglacial experiments indicate an enhanced seasonality with warmer boreal summer and colder boreal winter, especially over the Northern Hemisphere continents. This change is due to the redistributed seasonal solar insolation. A northward shift of the ITCZ is observed in both the mid-Holocene and the last interglacial compared to the present day, with wetter and drier conditions over the northern and southern edge of the tropical rain belt, respectively, accompanied by expansion and intensification of Northern Hemisphere monsoon. The increased monsoon precipitation over the main Northern Hemisphere monsoon domains (i.e., North America, North Africa, and South Asia) is contributed by the dynamic component of the moisture budget, which is related to changes in the atmospheric mean flow, while the thermodynamic term (associated with changes in relative humidity) plays a minor role. In terms of the atmospheric circulation, we find in both model versions a slowdown and northward shift of the Northern Hemisphere Hadley cell, linked with a smaller subtropical-to-equator temperature gradient. The Walker circulation, including the Pacific Walker cell and Indian Walker cell, also experiences a pronounced change. Both models identify a westward displacement in the totality of the Walker circulation as well as a

Unauthenticated | Downloaded 12/20/22 12:13 PM UTC

weakening in the Indian Walker cell, except that the mid-Holocene experiment performed by AWIESM2 shows no clear shift in the major rising branch of Walker circulation. Finally, increased instability of upper seawater at the North Atlantic contributes to an enhancement of AMOC in MH and LIG with respect to preindustrial simulated by AWIESM1. For AWIESM2 simulations, North Atlantic seawater in the MH is represented by cooling and warming at upper and deep ocean respectively, which leads to increased instability of the whole water column, while the LIG shows a more stable North Atlantic compared to preindustrial, evidenced in the increased seawater density gradient from upper to deep layers. In addition, the anomalous westerlies resembling the NAO pattern over the North Atlantic subpolar region can be superimposed on changes in AMOC.

We expect that our contribution will help to further complete the overview of PMIP4 results, and our data can be used in further studies for model–data or model–model comparison.

Acknowledgments. The present study is supported by the National Science Foundation of China (NSFC) (Grant 42206256), the Alfred Wegener Institute, the Helmholtz Center for Polar and Marine Research, and the German Federal Ministry of Education and Science (BMBF) PalMod II WP 3.3 (Grant 01LP1924B). The simulations were conducted on the Deutsche Klimarechenzentrum (DKRZ) and the AWI supercomputer (Ollie). The authors would like to acknowledge Roberta D'Agostino for providing the scripts for analyzing the moisture decomposition budget. The authors declare that no competing interests exist.

Data availability statement. The raw data related to the present study are available from https://doi.org/10.5281/zenodo.6539551.

REFERENCES

Bartlein, P. J., and S. L. Shafer, 2019: Paleo calendar-effect adjustments in time-slice and transient climate-model simulations (PaleoCalAdjust v1.0): Impact and strategies for data analysis. *Geosci. Model Dev.*, **12**, 3889–3913, https://doi.org/10.5194/gmd-12-3889-2019.

——, and Coauthors, 2011: Pollen-based continental climate reconstructions at 6 and 21 ka: A global synthesis. *Climate Dyn.*, **37**, 775–802, https://doi.org/10.1007/s00382-010-0904-1.

Berger, A., 1977: Long-term variations of the Earth's orbital elements. *Celestial Mech.*, **15**, 53–74, https://doi.org/10.1007/BF01229048.

Boos, W. R., and R. L. Korty, 2016: Regional energy budget control of the intertropical convergence zone and application to mid-Holocene rainfall. *Nat. Geosci.*, **9**, 892–897, https://doi.org/10.1038/ngeo2833.

Braconnot, P., and Coauthors, 2007: Results of PMIP2 coupled simulations of the Mid-Holocene and Last Glacial Maximum—Part 2: Feedbacks with emphasis on the location of the ITCZ and mid- and high latitudes heat budget. *Climate Past*, **3**, 279–296, https://doi.org/10.5194/cp-3-279-2007.

Brierley, C. M., and Coauthors, 2020: Large-scale features and evaluation of the PMIP4-CMIP6 midHolocene simulations. *Climate Past*, **16**, 1847–1872, https://doi.org/10.5194/cp-16-1847-2020.

Buiron, D., and Coauthors, 2011: TALDICE-1 age scale of the Talos Dome deep ice core, East Antarctica. *Climate Past*, **7** (1), 1–16, https://doi.org/10.5194/cp-7-1-2011.

Chang, C., and T. Li, 2000: A theory for the tropical tropospheric biennial oscillation. *J. Atmos. Sci.*, **57**, 2209–2224, https://doi.org/10.1175/1520-0469(2000)057<2209:ATFTTT>2.0.CO;2.

Chervin, R. M., and L. M. Druyan, 1984: The influence of ocean surface temperature gradient and continentality on the Walker circulation. Part I: Prescribed tropical changes. *Mon. Wea. Rev.*, **112**, 1510–1523, https://doi.org/10.1175/1520-0493(1984)112<1510:TIOOST>2.0.CO;2.

Chou, C., J. D. Neelin, and H. Su, 2001: Ocean–atmosphere–land feedbacks in an idealized monsoon. *Quart. J. Roy. Meteor. Soc.*, **127**, 1869–1891, https://doi.org/10.1002/qj.49712757602.

Cornejo-Garrido, A. G., and P. H. Stone, 1977: On the heat balance of the Walker circulation. *J. Atmos. Sci.*, **34**, 1155–1162, https://doi.org/10.1175/1520-0469(1977)034<1155:OTHBOT>2.0.CO;2.

D'Agostino, R., J. Bader, S. Bordoni, D. Ferreira, and J. Jungclaus, 2019: Northern Hemisphere monsoon response to mid-Holocene orbital forcing and greenhouse gas-induced global warming. *Geophys. Res. Lett.*, **46**, 1591–1601, https://doi.org/10.1029/2018GL081589.

Danabasoglu, G., and Coauthors, 2014: North Atlantic simulations in Coordinated Ocean-ice Reference Experiments phase II (core-II). Part I: Mean states. *Ocean Modell.*, **73**, 76–107, https://doi.org/10.1016/j.ocemod.2013.10.005.

Danilov, S., G. Kivman, and J. Schröter, 2004: A finite-element ocean model: Principles and evaluation. *Ocean Modell.*, **6**, 125–150, https://doi.org/10.1016/S1463-5003(02)00063-X.

——, Q. Wang, R. Timmermann, N. Iakovlev, D. Sidorenko, M. Kimmritz, T. Jung, and J. Schröter, 2015: Finite-Element Sea Ice Model (FESIM), version 2. *Geosci. Model Dev.*, **8**, 1747–1761, https://doi.org/10.5194/gmd-8-1747-2015.

——, D. Sidorenko, Q. Wang, and T. Jung, 2017: The Finite-Volume Sea Ice–Ocean Model (FESOM2). *Geosci. Model Dev.*, **10**, 765–789, https://doi.org/10.5194/gmd-10-765-2017.

Drake, N. A., R. M. Blench, S. J. Armitage, C. S. Bristow, and K. H. White, 2011: Ancient watercourses and biogeography of the Sahara explain the peopling of the desert. *Proc. Natl. Acad. Sci. USA*, **108**, 458–462, https://doi.org/10.1073/pnas.1012231108.

Dutton, A., J. M. Webster, D. Zwartz, K. Lambeck, and B. Wohlfarth, 2015: Tropical tales of polar ice: Evidence of last interglacial polar ice sheet retreat recorded by fossil reefs of the granitic Seychelles islands. *Quat. Sci. Rev.*, **107**, 182–196, https://doi.org/10.1016/j.quascirev.2014.10.025.

Eden, C., and J. Willebrand, 2001: Mechanism of interannual to decadal variability of the North Atlantic circulation. *J. Climate*, **14**, 2266–2280, https://doi.org/10.1175/1520-0442(2001)014<2266:MOITDV>2.0.CO;2.

Fischer, N., and J. Jungclaus, 2010: Effects of orbital forcing on atmosphere and ocean heat transports in Holocene and Eemian climate simulations with a comprehensive Earth system model. *Climate Past*, **6**, 155–168, https://doi.org/10.5194/cp-6-155-2010.

Flückiger, J., E. Monnin, B. Stauffer, J. Schwander, T. F. Stocker, J. Chappellaz, D. Raynaud, and J.-M. Barnola, 2002: High-resolution Holocene N_2O ice core record and its relationship with CH_4 and CO_2. *Global Biogeochem. Cycles*, **16**, 1010, https://doi.org/10.1029/2001GB001417.

Unauthenticated | Downloaded 12/20/22 12:13 PM UTC

Frajka-Williams, E., and Coauthors, 2019: Atlantic meridional overturning circulation: Observed transport and variability. *Front. Mar. Sci.*, **6**, 260, https://doi.org/10.3389/fmars.2019.00260.

Funder, S., and Coauthors, 2011: A 10,000-year record of Arctic Ocean sea-ice variability—View from the beach. *Science*, **333**, 747–750, https://doi.org/10.1126/science.1202760.

Ganachaud, A., and C. Wunsch, 2000: Improved estimates of global ocean circulation, heat transport and mixing from hydrographic data. *Nature*, **408**, 453–457, https://doi.org/10.1038/35044048.

Garratt, J., 1992: *The Atmospheric Boundary Layer*. Cambridge University Press, 316 pp.

Gent, P. R., and J. C. McWilliams, 1990: Isopycnal mixing in ocean circulation models. *J. Phys. Oceanogr.*, **20**, 150–155, https://doi.org/10.1175/1520-0485(1990)020<0150:IMIOCM>2.0.CO;2.

Hanslik, D., M. Jakobsson, J. Backman, S. Björck, E. Sellén, M. O'Regan, E. Fornaciari, and G. Skog, 2010: Quaternary Arctic Ocean sea ice variations and radiocarbon reservoir age corrections. *Quat. Sci. Rev.*, **29**, 3430–3441, https://doi.org/10.1016/j.quascirev.2010.06.011.

Hopcroft, P. O., P. J. Valdes, A. B. Harper, and D. J. Beerling, 2017: Multi vegetation model evaluation of the green Sahara climate regime. *Geophys. Res. Lett.*, **44**, 6804–6813, https://doi.org/10.1002/2017GL073740.

Hunke, E. C., and J. K. Dukowicz, 1997: An elastic–viscous–plastic model for sea ice dynamics. *J. Phys. Oceanogr.*, **27**, 1849–1867, https://doi.org/10.1175/1520-0485(1997)027<1849:AEVPMF>2.0.CO;2.

Jiang, D., Z. Tian, and X. Lang, 2015: Mid-Holocene global monsoon area and precipitation from PMIP simulations. *Climate Dyn.*, **44**, 2493–2512, https://doi.org/10.1007/s00382-014-2175-8.

Joshi, M. M., J. M. Gregory, M. J. Webb, D. M. Sexton, and T. C. Johns, 2008: Mechanisms for the land/sea warming contrast exhibited by simulations of climate change. *Climate Dyn.*, **30**, 455–465, https://doi.org/10.1007/s00382-007-0306-1.

Joussaume, S., and P. Braconnot, 1997: Sensitivity of paleoclimate simulation results to season definitions. *J. Geophys. Res.*, **102**, 1943–1956, https://doi.org/10.1029/96JD01989.

Kageyama, M., and Coauthors, 2018: The PMIP4 contribution to CMIP6—Part 1: Overview and over-arching analysis plan. *Geosci. Model Dev.*, **11**, 1033–1057, https://doi.org/10.5194/gmd-11-1033-2018.

——, and Coauthors, 2021a: A multi-model CMIP6-PMIP4 study of Arctic sea ice at 127 ka: Sea ice data compilation and model differences. *Climate Past*, **17**, 37–62, https://doi.org/10.5194/cp-17-37-2021.

——, and Coauthors, 2021b: The PMIP4 Last Glacial Maximum experiments: Preliminary results and comparison with the PMIP3 simulations. *Climate Past*, **17**, 1065–1089, https://doi.org/10.5194/cp-17-1065-2021.

Kang, S. M., S.-P. Xie, Y. Shin, H. Kim, Y.-T. Hwang, M. F. Stuecker, B. Xiang, and M. Hawcroft, 2020: Walker circulation response to extratropical radiative forcing. *Sci. Adv.*, **6**, eabd3021, https://doi.org/10.1126/sciadv.abd3021.

Köhl, A., 2005: Anomalies of meridional overturning: Mechanisms in the North Atlantic. *J. Phys. Oceanogr.*, **35**, 1455–1472, https://doi.org/10.1175/JPO2767.1.

Köhler, P., C. Nehrbass-Ahles, J. Schmitt, T. F. Stocker, and H. Fischer, 2017: A 156 kyr smoothed history of the atmospheric greenhouse gases CO_2, CH_4, and N_2O and their radiative forcing. *Earth Syst. Sci. Data*, **9**, 363–387, https://doi.org/10.5194/essd-9-363-2017.

Kukla, G. J., and Coauthors, 2002: Last interglacial climates. *Quat. Res.*, **58**, 2–13, https://doi.org/10.1006/qres.2001.2316.

Kutzbach, J. E., and Z. Liu, 1997: Response of the African monsoon to orbital forcing and ocean feedbacks in the middle Holocene. *Science*, **278**, 440–443, https://doi.org/10.1126/science.278.5337.440.

Large, W. G., J. C. McWilliams, and S. C. Doney, 1994: Oceanic vertical mixing: A review and a model with a nonlocal boundary layer parameterization. *Rev. Geophys.*, **32**, 363–403, https://doi.org/10.1029/94RG01872.

Latif, M., C. Böning, J. Willebrand, A. Biastoch, J. Dengg, N. Keenlyside, U. Schweckendiek, and G. Madec, 2006: Is the thermohaline circulation changing? *J. Climate*, **19**, 4631–4637, https://doi.org/10.1175/JCLI3876.1.

Lau, K., and S. Yang, 2003: Walker circulation. *Encyclopedia of Atmospheric Sciences*, Springer, 797–798.

Lin, S.-J., and R. B. Rood, 1996: Multidimensional flux-form semi-Lagrangian transport schemes. *Mon. Wea. Rev.*, **124**, 2046–2070, https://doi.org/10.1175/1520-0493(1996)124<2046:MFFSLT>2.0.CO;2.

Lohmann, G., M. Butzin, N. Eissner, X. Shi, and C. Stepanek, 2020: Abrupt climate and weather changes across time scales. *Paleoceanogr. Paleoclimatol.*, **35**, e2019PA003782, https://doi.org/10.1029/2019PA003782.

Lott, F., 1999: Alleviation of stationary biases in a GCM through a mountain drag parameterization scheme and a simple representation of mountain lift forces. *Mon. Wea. Rev.*, **127**, 788–801, https://doi.org/10.1175/1520-0493(1999)127<0788:AOSBIA>2.0.CO;2.

Loveland, T. R., B. C. Reed, J. F. Brown, D. O. Ohlen, Z. Zhu, L. Yang, and J. W. Merchant, 2000: Development of a global land cover characteristics database and IGBP DISCover from 1 km AVHRR data. *Int. J. Remote Sens.*, **21**, 1303–1330, https://doi.org/10.1080/014311600210191.

Lu, Z., P. A. Miller, Q. Zhang, Q. Zhang, D. Wårlind, L. Nieradzik, J. Sjolte, and B. Smith, 2018: Dynamic vegetation simulations of the mid-Holocene green Sahara. *Geophys. Res. Lett.*, **45**, 8294–8303, https://doi.org/10.1029/2018GL079195.

Lunt, D., and Coauthors, 2013: A multi-model assessment of last interglacial temperatures. *Climate Past*, **9**, 699–717, https://doi.org/10.5194/cp-9-699-2013.

Merlis, T. M., T. Schneider, S. Bordoni, and I. Eisenman, 2013: Hadley circulation response to orbital precession. Part I: Aquaplanets. *J. Climate*, **26**, 740–753, https://doi.org/10.1175/JCLI-D-11-00716.1.

Möbis, B., and B. Stevens, 2012: Factors controlling the position of the intertropical convergence zone on an aquaplanet. *J. Adv. Model. Earth Syst.*, **4**, M00A04, https://doi.org/10.1029/2012MS000199.

Monnin, E., and Coauthors, 2004: Evidence for substantial accumulation rate variability in Antarctica during the Holocene, through synchronization of CO_2 in the Taylor Dome, Dome C and DML ice cores. *Earth Planet. Sci. Lett.*, **224**, 45–54, https://doi.org/10.1016/j.epsl.2004.05.007.

Müller, J., K. Werner, R. Stein, K. Fahl, M. Moros, and E. Jansen, 2012: Holocene cooling culminates in sea ice oscillations in Fram Strait. *Quat. Sci. Rev.*, **47**, 1–14, https://doi.org/10.1016/j.quascirev.2012.04.024.

Nikolova, I., Q. Yin, A. Berger, U. Singh, and M. Karami, 2012: The last interglacial (Eemian) climate simulated by LOVECLIM

Unauthenticated | Downloaded 12/20/22 12:13 PM UTC

and CCSM3. *Climate Past Discuss.*, **8**, 5293–5340, https://doi.org/10.5194/cpd-8-5293-2012.

Nordeng, T. E., 1994: Extended versions of the convective parametrization scheme at ECMWF and their impact on the mean and transient activity of the model in the tropics. ECMWF Tech. Memo. 206, 41 pp., https://doi.org/10.21957/e34xwhysw.

North Greenland Ice Core Project Members, 2004: High-resolution record of the Northern Hemisphere climate extending into the last interglacial period. *Nature*, **431**, 147–151, https://doi.org/10.1038/nature02805.

Otto-Bliesner, B. L., and Coauthors, 2017: The PMIP4 contribution to CMIP6—Part 2: Two interglacials, scientific objective and experimental design for Holocene and Last Interglacial simulations. *Geosci. Model Dev.*, **10**, 3979–4003, https://doi.org/10.5194/gmd-10-3979-2017.

——, and Coauthors, 2021: Large-scale features of last interglacial climate: Results from evaluating the lig127k simulations for the Coupled Model Intercomparison Project (CMIP6)–Paleoclimate Modeling Intercomparison Project (PMIP4). *Climate Past*, **17**, 63–94, https://doi.org/10.5194/cp-17-63-2021.

Owens, W. B., and P. Lemke, 1990: Sensitivity studies with a sea ice-mixed layer-pycnocline model in the Weddell Sea. *J. Geophys. Res.*, **95**, 9527–9538, https://doi.org/10.1029/JC095iC06p09527.

Park, H.-S., S.-J. Kim, A. L. Stewart, S.-W. Son, and K.-H. Seo, 2019: Mid-Holocene Northern Hemisphere warming driven by Arctic amplification. *Sci. Adv.*, **5**, eaax8203, https://doi.org/10.1126/sciadv.aax8203.

Parkinson, C. L., and W. M. Washington, 1979: A large-scale numerical model of sea ice. *J. Geophys. Res.*, **84**, 311–337, https://doi.org/10.1029/JC084iC01p00311.

Pfeiffer, M., and G. Lohmann, 2016: Greenland ice sheet influence on last interglacial climate: Global sensitivity studies performed with an atmosphere–ocean general circulation model. *Climate Past*, **12**, 1313–1338, https://doi.org/10.5194/cp-12-1313-2016.

Rackow, T., H. F. Goessling, T. Jung, D. Sidorenko, T. Semmler, D. Barbi, and D. Handorf, 2018: Towards multi-resolution global climate modeling with ECHAM6-FESOM. Part II: Climate variability. *Climate Dyn.*, **50**, 2369–2394, https://doi.org/10.1007/s00382-016-3192-6.

Raddatz, T., and Coauthors, 2007: Will the tropical land biosphere dominate the climate–carbon cycle feedback during the twenty-first century? *Climate Dyn.*, **29**, 565–574, https://doi.org/10.1007/s00382-007-0247-8.

Redi, M. H., 1982: Oceanic isopycnal mixing by coordinate rotation. *J. Phys. Oceanogr.*, **12**, 1154–1158, https://doi.org/10.1175/1520-0485(1982)012<1154:OIMBCR>2.0.CO;2.

Renoult, M., and Coauthors, 2020: A Bayesian framework for emergent constraints: Case studies of climate sensitivity with PMIP. *Climate Past*, **16**, 1715–1735, https://doi.org/10.5194/cp-16-1715-2020.

Roeckner, E., and Coauthors, 2004: The atmospheric general circulation model ECHAM5 Part II: Sensitivity of simulated climate to horizontal and vertical resolution. 64 pp., http://hdl.handle.net/11858/00-001M-0000-0012-00E5-5.

Schilt, A., M. Baumgartner, T. Blunier, J. Schwander, R. Spahni, H. Fischer, and T. F. Stocker, 2010: Glacial–interglacial and millennial-scale variations in the atmospheric nitrous oxide concentration during the last 800,000 years. *Quat. Sci. Rev.*, **29**, 182–192, https://doi.org/10.1016/j.quascirev.2009.03.011.

Schneider, R., J. Schmitt, P. Köhler, F. Joos, and H. Fischer, 2013: A reconstruction of atmospheric carbon dioxide and its stable carbon isotopic composition from the penultimate glacial maximum to the last glacial inception. *Climate Past*, **9**, 2507–2523, https://doi.org/10.5194/cp-9-2507-2013.

Scholz, P., G. Lohmann, Q. Wang, and S. Danilov, 2013: Evaluation of a Finite-Element Sea-Ice Ocean Model (FESOM) setup to study the interannual to decadal variability in the deep-water formation rates. *Ocean Dyn.*, **63**, 347–370, https://doi.org/10.1007/s10236-012-0590-0.

——, D. Kieke, G. Lohmann, M. Ionita, and M. Rhein, 2014: Evaluation of Labrador Sea water formation in a global finite-element sea-ice ocean model setup, based on a comparison with observational data. *J. Geophys. Res. Oceans*, **119**, 1644–1667, https://doi.org/10.1002/2013JC009232.

——, and Coauthors, 2019: Assessment of the Finite-Volume Sea Ice-Ocean Model (FESOM2.0)—Part 1: Description of selected key model elements and comparison to its predecessor version. *Geosci. Model Dev.*, **12**, 4875–4899, https://doi.org/10.5194/gmd-12-4875-2019.

Scussolini, P., and Coauthors, 2019: Agreement between reconstructed and modeled boreal precipitation of the last interglacial. *Sci. Adv.*, **5**, eaax7047, https://doi.org/10.1126/sciadv.aax7047.

Semtner, A. J., Jr., 1976: A model for the thermodynamic growth of sea ice in numerical investigations of climate. *J. Phys. Oceanogr.*, **6**, 379–389, https://doi.org/10.1175/1520-0485(1976)006<0379:AMFTTG>2.0.CO;2.

Shi, X., and G. Lohmann, 2016: Simulated response of the mid-Holocene Atlantic meridional overturning circulation in ECHAM6-FESOM/MPIOM. *J. Geophys. Res. Oceans*, **121**, 6444–6469, https://doi.org/10.1002/2015JC011584.

——, and ——, 2017: Sensitivity of open-water ice growth and ice concentration evolution in a coupled atmosphere–ocean–sea ice model. *Dyn. Atmos. Oceans*, **79**, 10–30, https://doi.org/10.1016/j.dynatmoce.2017.05.003.

——, ——, D. Sidorenko, and H. Yang, 2020: Early-Holocene simulations using different forcings and resolutions in AWI-ESM. *Holocene*, **30**, 996–1015, https://doi.org/10.1177/0959683620908634.

——, and Coauthors, 2022: Calendar effects on surface air temperature and precipitation based on model-ensemble equilibrium and transient simulations from PMIP4 and PACMEDY. *Climate Past*, **18**, 1047–1070, https://doi.org/10.5194/cp-18-1047-2022.

Sidorenko, D., and Coauthors, 2015: Towards multi-resolution global climate modeling with ECHAM6–FESOM. Part I: Model formulation and mean climate. *Climate Dyn.*, **44**, 757–780, https://doi.org/10.1007/s00382-014-2290-6.

——, and Coauthors, 2019: Evaluation of FESOM2.0 coupled to ECHAM6.3: Preindustrial and HighResMIP simulations. *J. Adv. Model. Earth Syst.*, **11**, 3794–3815, https://doi.org/10.1029/2019MS001696.

Skonieczny, C., and Coauthors, 2015: African humid periods triggered the reactivation of a large river system in Western Sahara. *Nat. Commun.*, **6**, 8751, https://doi.org/10.1038/ncomms9751.

Stevens, B., and Coauthors, 2013: Atmospheric component of the MPI-M Earth System Model: ECHAM6. *J. Adv. Model. Earth Syst.*, **5**, 146–172, https://doi.org/10.1002/jame.20015.

Talley, L. D., 2013: Closure of the global overturning circulation through the Indian, Pacific, and Southern Oceans: Schematics and transports. *Oceanography*, **26**, 80–97, https://doi.org/10.5670/oceanog.2013.07.

Tian, Z., T. Li, and D. Jiang, 2018: Strengthening and westward shift of the tropical Pacific Walker circulation during the mid-

Unauthenticated | Downloaded 12/20/22 12:13 PM UTC

Holocene: PMIP simulation results. *J. Climate*, **31**, 2283–2298, https://doi.org/10.1175/JCLI-D-16-0744.1.

Tiedtke, M., 1989: A comprehensive mass flux scheme for cumulus parameterization in large-scale models. *Mon. Wea. Rev.*, **117**, 1779–1800, https://doi.org/10.1175/1520-0493(1989)117<1779:ACMFSF>2.0.CO;2.

Timmermann, R., S. Danilov, J. Schröter, C. Böning, D. Sidorenko, and K. Rollenhagen, 2009: Ocean circulation and sea ice distribution in a finite element global sea ice–ocean model. *Ocean Modell.*, **27**, 114–129, https://doi.org/10.1016/j.ocemod.2008.10.009.

Turney, C. S., and R. T. Jones, 2010: Does the Agulhas Current amplify global temperatures during super-interglacials? *J. Quat. Sci.*, **25**, 839–843, https://doi.org/10.1002/jqs.1423.

Wang, Q., S. Danilov, and J. Schröter, 2008: Finite element ocean circulation model based on triangular prismatic elements, with application in studying the effect of topography representation. *J. Geophys. Res.*, **113**, C05015, https://doi.org/10.1029/2007JC004482.

——, ——, D. Sidorenko, R. Timmermann, C. Wekerle, X. Wang, T. Jung, and J. Schröter, 2014: The Finite Element Sea Ice-Ocean Model (FESOM) v.1.4: Formulation of an ocean general circulation model. *Geosci. Model Dev.*, **7**, 663–693, https://doi.org/10.5194/gmd-7-663-2014.

Wang, Y., and Coauthors, 2008: Millennial- and orbital-scale changes in the East Asian monsoon over the past 224,000 years. *Nature*, **451**, 1090–1093, https://doi.org/10.1038/nature06692.

Yang, H., G. Lohmann, J. Lu, E. J. Gowan, X. Shi, J. Liu, and Q. Wang, 2020a: Tropical expansion driven by poleward advancing midlatitude meridional temperature gradients. *J. Geophys. Res. Atmos.*, **125**, e2020JD033158, https://doi.org/10.1029/2020JD033158.

——, and Coauthors, 2020b: Poleward shift of the major ocean gyres detected in a warming climate. *Geophys. Res. Lett.*, **47**, e2019GL085868, https://doi.org/10.1029/2019GL085868.

——, J. Lu, Q. Wang, X. Shi, and G. Lohmann, 2022a: Decoding the dynamics of poleward shifting climate zones using aquaplanet model simulations. *Climate Dyn.*, **58**, 3513–3526, https://doi.org/10.1007/s00382-021-06112-0.

——, and Coauthors, 2022b: Impact of paleoclimate on present and future evolution of the Greenland Ice Sheet. *PLOS ONE*, **17**, e0259816, https://doi.org/10.1371/journal.pone.0259816.

Yin, Q., and A. Berger, 2015: Interglacial analogues of the Holocene and its natural near future. *Quat. Sci. Rev.*, **120**, 28–46, https://doi.org/10.1016/j.quascirev.2015.04.008.

Zhang, Q., and Coauthors, 2021: Simulating the mid-Holocene, last interglacial and mid-Pliocene climate with EC-EARTH3-LR. *Geosci. Model Dev.*, **14**, 1147–1169, https://doi.org/10.5194/gmd-14-1147-2021.

Unauthenticated | Downloaded 12/20/22 12:13 PM UTC